2019

ACOUSTIC GROUND SENSORS TO TRIANGULATE BOMB IMPACT IN SUPPORT OF AIRFIELD DAMAGE ASSESSMENT

Mutton, John O.

Monterey, CA; Naval Postgraduate School

NAVAL POSTGRADUATE SCHOOL

MONTEREY, CALIFORNIA

THESIS

ACOUSTIC GROUND SENSORS TO TRIANGULATE BOMB IMPACT IN SUPPORT OF AIRFIELD DAMAGE ASSESSMENT

by

John O. Mutton

June 2019

Thesis Advisor:	Gurminder Singh
Co-Advisor:	Fabio D. Alves
Second Reader:	Peter R. Ateshian

THIS PAGE INTENTIONALLY LEFT BLANK

REPORT DOCUMENTATION PAGE	*Form Approved OMB No. 0704-0188*

1. AGENCY USE ONLY *(Leave blank)*	**2. REPORT DATE** June 2019	**3. REPORT TYPE AND DATES COVERED** Master's thesis

4. TITLE AND SUBTITLE
ACOUSTIC GROUND SENSORS TO TRIANGULATE BOMB IMPACT IN SUPPORT OF AIRFIELD DAMAGE ASSESSMENT

5. FUNDING NUMBERS

6. AUTHOR(S) John O. Mutton

7. PERFORMING ORGANIZATION NAME(S) AND ADDRESS(ES)
Naval Postgraduate School
Monterey, CA 93943-5000

8. PERFORMING ORGANIZATION REPORT NUMBER

9. SPONSORING / MONITORING AGENCY NAME(S) AND ADDRESS(ES)
N/A

10. SPONSORING / MONITORING AGENCY REPORT NUMBER

11. SUPPLEMENTARY NOTES The views expressed in this thesis are those of the author and do not reflect the official policy or position of the Department of Defense or the U.S. Government.

12a. DISTRIBUTION / AVAILABILITY STATEMENT
Approved for public release. Distribution is unlimited.

12b. DISTRIBUTION CODE
A

13. ABSTRACT (maximum 200 words)

Airfield damage repair (ADR) is a critical function in restoring damaged airfields after an adversary attack. Before ADR can commence, airfield damage assessment (ADA)—a labor- and time-intensive process—must be conducted. Maintaining airfields in wartime is especially difficult since runways are large, and the presence of unexploded ordnance or chemical weapons poses a safety hazard to ground personnel conducting the damage assessment. To accelerate the ADA process, a network of micro-electro-mechanical (MEM) sensors are used to capture the sound of the explosion and triangulate bomb impacts on the airfield autonomously and instantaneously. This autonomous process can be faster than current methods and can keep personnel safe by limiting them from surveying the airfield. We test several MEM sensors and evaluate localization accuracy, networking capability, simplicity of use, and cost to improve the process. Using a combination of MEM sensors, radio frequency transceivers, GPS modules, microcontrollers, and MATLAB code, we demonstrate that bomb impacts can be triangulated and displayed on an interface for supporting the ADA mission.

14. SUBJECT TERMS
triangulation, acoustic ground sensor, sound localization, Arduino, mobile network, airfield damage repair (ADR), airfield damage assessment (ADA), direction finding (DF) sensor, microelectromechanical

15. NUMBER OF PAGES
111

16. PRICE CODE

17. SECURITY CLASSIFICATION OF REPORT	**18. SECURITY CLASSIFICATION OF THIS PAGE**	**19. SECURITY CLASSIFICATION OF ABSTRACT**	**20. LIMITATION OF ABSTRACT**
Unclassified	Unclassified	Unclassified	UU

NSN 7540-01-280-5500

Standard Form 298 (Rev. 2-89)
Prescribed by ANSI Std. 239-18

THIS PAGE INTENTIONALLY LEFT BLANK

Approved for public release. Distribution is unlimited.

ACOUSTIC GROUND SENSORS TO TRIANGULATE BOMB IMPACT IN SUPPORT OF AIRFIELD DAMAGE ASSESSMENT

John O. Mutton
Captain, United States Marine Corps
BS, U.S. Naval Academy, 2012

Submitted in partial fulfillment of the
requirements for the degree of

MASTER OF SCIENCE IN COMPUTER SCIENCE

from the

NAVAL POSTGRADUATE SCHOOL
June 2019

Approved by: Gurminder Singh
Advisor

Fabio D. Alves
Co-Advisor

Peter R. Ateshian
Second Reader

Peter J. Denning
Chair, Department of Computer Science

THIS PAGE INTENTIONALLY LEFT BLANK

ABSTRACT

Airfield damage repair (ADR) is a critical function in restoring damaged airfields after an adversary attack. Before ADR can commence, airfield damage assessment (ADA)—a labor- and time-intensive process—must be conducted. Maintaining airfields in wartime is especially difficult since runways are large, and the presence of unexploded ordnance or chemical weapons poses a safety hazard to ground personnel conducting the damage assessment. To accelerate the ADA process, a network of micro-electro-mechanical (MEM) sensors are used to capture the sound of the explosion and triangulate bomb impacts on the airfield autonomously and instantaneously. This autonomous process can be faster than current methods and can keep personnel safe by limiting them from surveying the airfield. We test several MEM sensors and evaluate localization accuracy, networking capability, simplicity of use, and cost to improve the process. Using a combination of MEM sensors, radio frequency transceivers, GPS modules, microcontrollers, and MATLAB code, we demonstrate that bomb impacts can be triangulated and displayed on an interface for supporting the ADA mission.

THIS PAGE INTENTIONALLY LEFT BLANK

TABLE OF CONTENTS

I. INTRODUCTION....1
A. CONTEXT AND MOTIVATION....1
B. RESEARCH FOCUS....2
C. PROJECT SCOPE....2
D. BENEFITS OF STUDY....3
E. THESIS ORGANIZATION....3

II. BACKGROUND INFORMATION....5
A. AIRFIELD DAMAGE ASSESSMENT AND AIRFIELD DAMAGE REPAIR....5
1. Importance and Necessity for ADA and ADR....6
B. CURRENT STANDARD OPERATING PROCEDURES....6
1. Organization United States Air Force....7
2. Organization United States Marine Corps....7
3. Airfield Damage Assessment Process....8
C. TECHNOLOGIES USED FOR ADA....15
1. iFerret and Super Bullseye....15
2. Geospatial Expeditionary Planning Tool....17
3. Previous Work at NPS....18
D. MICROELECTROMECHANICAL SENSORS....20
E. SMALL MICROCONTROLLER DEVICES....20
F. SUMMARY....21

III. HARDWARE SELECTION AND SYSTEM DESIGN....23
A. SYSTEM ARCHITECTURE OVERVIEW AND GOAL....23
B. SYSTEM COMPONENTS....24
1. MEMS Direction Finding Acoustic Sensor....24
2. RF Transceiver Module....30
3. Global Positioning System Module....36
4. Microcontroller....38
5. Sensor Node Cost Estimation....39
C. TRIANGULATION ALGORITHM FOR LOCALIZING SOUND SOURCE....41
1. Python PyGeodesy Triangulation....45
2. MATLAB Mapping Toolbox....46
D. SYSTEM PROCESS AND INFORMATION FLOW....47
E. SUMMARY....51

IV. IMPLEMENTATION AND TESTING 53
A. PURPOSE OF EXPERIMENTATION 53
1. Measurements and Analysis 53
B. EXPERIMENTATION 56
1. Anechoic Chamber Calibration Testing 56
2. Anechoic Chamber Triangulation Experiment 61
3. Open Environment Testing 69
C. SUMMARY 74

V. CONCLUSION 77
A. SUMMARY 77
B. CONCLUSIONS 77
C. RECOMMENDATIONS FOR FUTURE WORK 78

APPENDIX. SOURCE CODE 81

LIST OF REFERENCES 83

INITIAL DISTRIBUTION LIST 87

LIST OF FIGURES

Figure 1. Multiple damage and UXO assessment. Source: DAF (2016). 12

Figure 2. Runway damage listing and potential MOS. Source: DAF (2012). 14

Figure 3. iFerret static position camera. Source: Stratech Systems Limited (n.d.). 16

Figure 4. GeoExPT damage plotting feature. Source: USG (2018). 17

Figure 5. GeoExPT MOS selection feature. Source: USG (2018). 18

Figure 6. Arduino Uno Rev3. Source: Arduino (2018). 21

Figure 7. Arduino Nano. Source: Arduino (2018). 21

Figure 8. Sensor network implementation during ADA 23

Figure 9. Mechanical model simulating the *Ormia ochracea* ear organs. Source: Miles et al. (1996). 26

Figure 10. Schematic of (a) mechanical structure of fly's eardrums and (b) vibration modes under sound excitation. Source: Karunasiri et al. (2017). 27

Figure 11. Layout of MEMS directional acoustic sensor. Source: Wilmott et al. (2016). 28

Figure 12. Arrangement of two MEMS DF sensors canted at θ_{off}. Source: Wilmott et al. (2016). 29

Figure 13. Dual sensor assembly. Source: Karunasiri et al. (2017). 30

Figure 14. Nordic semiconductor nRF24L01+ transceiver module. Source: Last Minute Engineers (n.d.-a). 31

Figure 15. nRF24L01+ frequency channel. Source: Last Minute Engineers (n.d.-a). 32

Figure 16. Basic implementation of the power amplifier and low noise amplifier for the transceiver. Source: Last Minute Engineers (n.d.-a). 34

Figure 17. nRF24L01+ multiceiver network diagram. Source: Last Minute Engineers (n.d.-a). 35

Figure 18. Enhanced shockburst packet structure. Source: Last Minute Engineers (n.d.-a). 36

Figure 19. ublox NEO-6M GPS module. Source: u-blox (2011). 37

Figure 20. Circuit overview for the sensor node. 39

Figure 21. Sensor node design 40

Figure 22. Triangulation determined by intersection of two bearings from two known locations 42

Figure 23. Horizontal position is represented by the vertical vector from the surface tangent plane on the Earth model. Source: Gade (2010). 46

Figure 24. MATLAB mapping interface displaying the locations of the sensors 48

Figure 25. Ground sensor node transmission of ID number, latitude, longitude, and bearing to the hub receiver node 49

Figure 26. MATLAB mapping interface displaying bearing angle lines 50

Figure 27. MATLAB mapping interface using intersection function to determining latitude and longitude of intersection 51

Figure 28. Precision and accuracy with regard to the ground sensor network system. Source: Carlson (2002). 55

Figure 29. Schematic of the NPS anechoic chamber room setup for calibration testing 57

Figure 30. Images of the NPS anechoic room setup 57

Figure 31. Graph comparing the actual angle and the measured angle for sensor node 1 59

Figure 32. Graph comparing the actual angle and the measured angle for sensor node 2 61

Figure 33. Schematic of the triangulation experiment in the anechoic chamber 62

Figure 34. Image of the triangulation experiment in the anechoic chamber 62

Figure 35. Image of the triangulation experiment in the anechoic chamber 63

Figure 36. Triangulation output of test 1, trial 1 performed in MATLAB 64

Figure 37. Overall results from MATLAB program triangulating the sound source for test 1, trials 1-4.....65

Figure 38. Triangulation output of test 2, trial 1 performed in MATLAB.....66

Figure 39. Overall results from MATLAB program triangulating the sound source for test 2, trials 1-4.....67

Figure 40. Triangulation output of test 3, trial 1 performed in MATLAB.....68

Figure 41. Overall results from MATLAB program triangulating the sound source for test 3, trials 1-4.....69

Figure 42. Overview of the general setup for the outside tests of the sensor system 70

Figure 43. Aerial view of the measured points calculated by triangulation compared with the actual location 71

Figure 44. Aerial view of the measured points calculated by triangulation compared with the actual location 73

THIS PAGE INTENTIONALLY LEFT BLANK

LIST OF TABLES

Table 1. Airfield damage types. 9

Table 2. Assessment priorities. Source: DAF (2016). 13

Table 3. Sensor node estimated price....41

Table 4. Hub node estimated price....41

Table 5. Decimal degree precision and conversion to distance. Source: U.S. Naval Academy [USNA] (2017). 54

Table 6. Data results comparing the measured angle and actual angle for sensor node 1....59

Table 7. Data results comparing the measured angle and actual angle for sensor node 2....60

Table 8. Results of anechoic chamber test 1 to include bearings from sensor nodes, measured location, and distance between measured and actual 65

Table 9. Results of anechoic chamber test 2 to include bearings from sensor nodes, measured location, and distance between measured and actual 67

Table 10. Results of anechoic chamber test 3 to include bearings from sensor nodes, measured location, and distance between measured and actual 69

Table 11. Results of the measured coordinates compared with the actual coordinates and the distance between the two points 72

Table 12. Results of the measured coordinates compared with the actual coordinates and the distance between the two points 74

THIS PAGE INTENTIONALLY LEFT BLANK

LIST OF ACRONYMS AND ABBREVIATIONS

ADA	airfield damage assessment
ADR	airfield damage repair
ADAT	airfield damage assessment team
AGSOC	aviation ground support operations center
BRAAT	base recovery after attack
COTS	commercial off the shelf
CPU	central processing unit
CRC	cyclic redundancy check
DART	damage assessment response team
DF	direction finding
DoD	Department of Defense
EOC	Emergency Operations Center
EOD	explosive ordnance disposal
FOD	foreign object debris
FOL	forward operating location
FSK	frequency shift key
GeoExPT	Geospatial Expeditionary Planning Tool
GFSK	gaussian frequency-shift keying
GIS	geographic information system
GPIO	general purpose input-output
GPS	global positioning system
HADR	humanitarian assistance and disaster relief
HARM	high-aspect-ratio micromachining
ICC	installation control center
IDE	Integrated Development Environment
LIDAR	light detection and ranging
LNA	low-noise amplifier
MAOS	minimum airfield operating strip
MEMS	microelectromechanical systems
MOB	main operating base

MOS	minimum operating strip
MWSS	Marine Wing Support Squadron
NBC	nuclear, biological, and chemical
PA	power amplifier
PCF	packet control field
PLA	polylactic acid
RADAS	rapid airfield damage assessment system
RF	radio frequency
RRR	rapid runway repair
SPI	serial peripheral interface
TTFF	time-to-first-fix
UAV	unmanned aerial vehicles
UXO	unexploded ordnance

EXECUTIVE SUMMARY

The U.S. military conducts a wide range of power projection across the globe, including combat operations, peacetime operations and exercises, and humanitarian assistance and disaster relief. U.S. airpower plays a critical role in supporting and executing the strategic and tactical goals of the Department of Defense (DoD) through force projection and sustainment. Aviation operations provide assault support, reconnaissance and surveillance, electronic warfare, offensive air support, and anti-air warfare to support and sustain the warfighter and to impose our will on the enemy. Modern aircraft require an airfield or landing surface that provides support for launching and recovering aircraft, parking, fueling, arming, and other necessary aviation support. Interruption to aviation support affects the airpower capability to support operations that require airpower. Airfields are lucrative targets for the enemy knowing that damaging the aviation support infrastructure will hinder the air operations.

Adversaries today have the means to target our airfields to cause major damage. The ability to assess and restore the airfields is critical to sustaining the U.S. mission. Airfield Damage Repair (ADR) is the process of repairing airfield damage encompassing surfaces and support infrastructure so that aviation operations can continue. The proper execution and success of ADR depends on the accurate assessment of the damage. Airfield Damage Assessment (ADA) is the evaluation of damages including the runway and taxiway surfaces, facilities, and infrastructure of an airfield. The accurate and detailed assessment is very important in providing information that is used for determining the best course of action to repair the necessary damages to the airfield so that launch and recovery operations can resume. Damage assessment teams are deployed after an attack to survey and record damage location, type, size and if there is any unexploded ordnance (UXO). The current ADA process is time consuming and dangerous to the personnel conducting the assessment. Airfields can be very large with runways reaching 10,000 feet in length. Personnel are conducting surveys either on mounted or dismounted which will require much time to accurately report all damage. Also, the presence of UXO can slow down the

ADA process and also poses a danger to the assessment teams. The thoroughness and speed of ADA is important to the success of ADR and restoring the airfield to operational status.

The goal of this thesis is to develop a basic ground acoustic sensor network to triangulate bomb impacts autonomously and instantaneously and provide data to airfield's operation center to support the ADA process. The network system will be comprised of induvial ground sensor nodes that are equipped with a Microelectromechanical Systems (MEMS) direction finding (DF) acoustic sensor, an Arduino Uno Rev3 or Arduino Nano, global positioning system (GPS) module, and a transceiver module for communication. The Arduino controls all the processes that are being executed in the ground sensor node comprised of sound detection, GPS, and communication. The MEMS DF acoustic sensor, which has a resonant response, has been designed to provide a bearing to the sound blast. The GPS module provides the location of the ground sensor and with the bearing angle and known location of the sensor, the information will be transmitted using the transceiver module. The system design is comprised of low cost and low power commercial-off-the-shelf products that can be easily attainable and provide simplicity in the architecture.

All data is sent to a hub receiver node where calculations and a mapping display is created. Using a triangulation algorithm based on the latitude and longitude of two known points with each point providing a bearing to a sound source, an estimated location of the bomb impact is calculated. MATLAB is used for the calculations and mapping since it can integrate with the data that is processed by Arduino. With MATLAB, the algorithm processes the data collected from the ground sensor nodes to calculate the position of the bomb impact and provide the latitude and longitude of that location. The MATLAB mapping toolbox displays each sensor's location on a map and when sound detection has occurred provides a bearing line to the sound source. With this information, the map provides a visual representation of the area which is helpful in the ADA process.

The goal of the experimentation was to test the accuracy of the ground sensor nodes in detecting and transmitting data to the hub receiver node in order to test the precision of the triangulation calculation and mapping. The system was tested in an outside environment but was restricted regarding to creating an actual explosion or live ammunition. To test the system, a loud speaker was used to play a bomb explosion and

moved to different locations and at varying distances to simulate an environment that has experience bomb impacts. Testing was conducted in an anechoic chamber to ensure accuracy of the sensor nodes before doing outside experiments to simulate an operational environment. The sound source location is compared with the experimental location value that is calculated in MATLAB. Using Haversine's formula, the distance between the actual location and estimated location is calculated to show accuracy.

From the experiments using the loud speaker to simulate a bomb explosion in the anechoic chamber and outside environment, the system demonstrated it can accurately detect, transmit data, and triangulate the location of a bomb blast. Multiple test trials were conducted testing two sensor nodes to validate the accuracy and compare the measured results with the actual values. A 200-inch by 100-inch grid was created in the anechoic chamber in which three different tests with four trials per a test was done. The experimentation showed accuracy and precision with the system with the longest distance being 11 inches between the actual location and measured location. Also, all measured locations were consistent and close to one another with sporadic outliers. Outside tests were done at the Naval Postgraduate School to test the system with environmental factors added. Outside tests also showed similar results to the anechoic chamber with accurate measured locations less than 20 feet away from the actual location. The system produced constant triangulation location points that were in proximity to one another and close to the actual location of the sound source.

From the experimental results of the ground sensor network, it is possible to conclude that we can accurately triangulate a bomb impact using the low-cost equipment and software combination described in this document. Though the research provided good data analysis of the system, there are recommendations to improve the system. Though these sensors are positioned away from the targeted areas on an airfield, the sensors are still subjugated to bomb explosions which can damage them. The sensors will be an outside environment and susceptible to the inclement weather and military operations. Some type of enclosure to protect the components from these aspects will ensure the longevity and accuracy of the device. Another recommendation is the ability for the ground sensors to determine distinction between multiple impact sounds and to provide that data accurately

to the hub node. If an airfield is to come under attack, there will more likely be multiple munitions that will impact the runway. The system lays the groundwork for integrating MEMS DF acoustic sensors into a network that can be used to accurately triangulate and provide location of bomb impacts. With the recommendations provided and the possibility of integrating the design with other unmanned equipment such as Unmanned Aerial Vehicles (UAVs), the system can reduce the process time and increase the accuracy of ADA while keeping U.S. military personnel safe.

ACKNOWLEDGMENTS

I would like to thank Dr. Gurminder Singh, Dr. Fabio Alves, Dr. Gamani Karunasiri, and Professor Peter Ateshian for their guidance throughout this process. Additionally, I offer my gratitude to Charles Prince, Professor Peter Crooker, Jaehyun Park, and Dr. Renato Rabelo for helping me with the research and experimentation. Also, I would like to thank my parents, Tom Mutton and Debra Scott, and my brothers, Edwin and Paul, for their support throughout the years.

THIS PAGE INTENTIONALLY LEFT BLANK

I. INTRODUCTION

This chapter discusses Airfield Damage Assessment (ADA) and its importance to the United States (U.S.) military operations as well as problems with the ADA process as currently practiced by our military. The chapter presents the research focus and benefits that it provides to the Department of Defense (DoD).

A. CONTEXT AND MOTIVATION

Air power is vital to the success of military operations in the DoD as a variety of missions and roles rely on the aviation components of all branches. These missions include but are not limited to offensive air support, intelligence and reconnaissance, air assault support and logistics, and electronic warfare. Air power is not only used for combat operations but also delivers capabilities to humanitarian assistance and disaster relief (HADR), peace keeping missions, and training operations. To carry out successful aviation operations and to project air power, U.S. military forces must have functional and operational airfields that can launch and recover aircrafts and provide the necessary logistics to maintain and upkeep aircrafts. Airfields are a prime target for enemy combatants since disruption in aviation operations can negatively affect most other military operations. ADA is the process of assessing damage to an airfield so that estimations and requirements can be determined to conduct repair on the airfield. The current processes used in ADA are time consuming, labor intensive and hazardous due to the unexploded ordnance (UXO) and the enemy threat, but today's technology can be used to improve current procedures of ADA, which in turn improves the airfield recovery time.

Before Airfield Damage Repair (ADR) can begin repair an airfield, ADA must provide an overview of the damage sustained. The current ADA process is split into two phases: Phase I: initial reconnaissance and Phase II: detailed reconnaissance. Phase I provides a quick assessment of the airfield damage while Phase II is more detailed and provides data back to the operations center. This data is used for calculations for engineer operations to repair the airfield and determine available flight lines that can be used to maintain aviation operations. Current procedures of Phase II are conducted either by foot

patrols or in armored vehicles, which are slow due to the large sizes of airfields and hazards to the personnel performing the assessment. The efficiency and speed of ADA is critical to the success of ADR because the time needed to conduct a proper assessment adds to the time for the restoration of the airfield. With the U.S. military present in many countries and occupying foreign airfields, a faster and more efficient ADA process benefits the success of maintaining and recovering airfields when attacked.

B. RESEARCH FOCUS

To improve the speed and accuracy of the ADA process, this research studies the use of acoustic sensors that can be deployed to detect and triangulate bomb impacts autonomously and instantaneously while an attack is in process. A low-cost, low-power and easily deployable network of integrated acoustic sensors that can accurately determine an impact location is a feasible solution. The network system can transmit data from each sensor node to an operations center where triangulation algorithms determine the location of the bomb impact and a mapping interface plots damage. The sensor network can improve the speed of ADA Phase I, which, in turns, decreases the time of Phase II since the impact locations have already been determined and mapped out for ground personnel to do detailed assessments.

C. PROJECT SCOPE

The focus of this project is to use and evaluate commercial-off-the-shelf (COTS) equipment that can be used to triangulate impact locations on airfield to support ADA. The equipment to be evaluated include microcontrollers, transceiver modules, and Global Positioning System (GPS) modules in conjunction with the use of Microelectromechanical Systems (MEMS) acoustic sensors that are researched and designed at the Physics Department, Naval Postgraduate School. COTS equipment used is readily available, low-cost, and open source documentation is helpful to integrate all the components of the design. The equipment needs to have a low-power requirement due to the operational environment and isolation from power sources. The communication unit of the sensor network is required to transmit and receive data wirelessly due to the remote location of airfields that are used by U.S. military forces.

D. BENEFITS OF STUDY

The system described in this research improves the capability of the ADA process which in turn improves recovery operations for airfield damage. The sensor network provides location of bomb impacts autonomously and concurrently while a base is under attack. This increases the speed and accuracy of Phase I of ADA and provides a detail overview of the damage location so that assessment teams are aware and can immediately deploy to locations for confirmation and estimation of the detailed damage. Another benefit that the system provides is that it reduces the risks to the assessment team personnel surveying the airfield. UXO can be present after an attack and in a hostile area, a potential enemy threat is possible placing the surveying teams in danger. With an accurate detection system deployed, damage locations are known, which can reduce the requirement for personnel to patrol the airfield during the assessment.

E. THESIS ORGANIZATION

This chapter has provided the motivation for the research for creating a ground acoustic sensor network. Chapter II provides background information about the ADA/ADR process and the importance it has for aviation operations in the U.S. military. The chapter reviews technologies that have been tested and used for ADA and addresses previous research conducted at the Naval Postgraduate School. The chapter finishes by providing information about MEMS sensors and microcontrollers that collect and process data.

Chapter III is a detailed overview of the network system designed for this thesis. It includes information about all equipment components that are integrated into the system and discusses the process flow for the collection and transmission of data from the source to the operations center. The system is composed of multiple sensor nodes that calculate a bearing angle to the sound source. With this bearing data, the sensor node transmits the bearing and sensor location to a hub node for triangulation calculations. Once the hub node receives data from at least two sensors, it calculates the location of the sound source and creates a map display.

Chapter IV presents our testing of the system in a controlled environment, followed by testing in a simulated operational environment. The chapter provides a detailed

depiction on how the system works and reacts when operated. Data collected during the test is used for analyzing and comparing accuracy of the sensor network.

Chapter V completes the research by providing conclusions and results of the network system implementation. The chapter highlights the system performance and presents future work recommendations to improve the system.

II. BACKGROUND INFORMATION

This chapter discusses the process and overview of ADA and ADR and the importance that it has in restoring airfield operations when an airbase has been damaged. The chapter also discusses current ADA procedures and the needs for new technology to improve the speed, accuracy, and efficiency of the process.

A. AIRFIELD DAMAGE ASSESSMENT AND AIRFIELD DAMAGE REPAIR

ADR is a critical function in restoring damaged airfields after an adversary attack or natural causes so that aviation operations can resume. A runway and the supporting infrastructure are attractive targets for an enemy force as damage to them can impede air operations. ADR "encompasses all actions required to rapidly prepare airfield operations surfaces and infrastructure to establish or sustain operations at a new forward operating location (FOL) or to recover operations at a main operating base (MOB) or FOL that has sustained damage from attack" (Department of the Air Force [DAF], 2012, p. 11). Before ADR can be started, ADA must be conducted. "Airfield damage assessment is the process of locating, classifying, and measuring airfield damage and unexploded explosive ordnance (UXO) after an attack" (DAF, 2016, p. 4). ADA is important because it provides the measurements and locations of damages on the airfield so that recovery teams and engineers can estimate materials needed and plan for reconstruction of the airfield.

ADA is categorized into two areas, the airfield damage assessment and facility/utility damage assessment. Airfield damage assessment include runways, taxiways, parking apron surfaces, runway infrastructure to include lighting, aircraft arresting systems utility lines, signage, navigational aids, and location of UXO (DAF, 2012). Facility/utility damage assessment includes the airbase facilities, infrastructure, and utility systems. This paper focuses on airfield damage assessment. The process of ADA is split into two phases: Phase I: initial reconnaissance and Phase II: detailed reconnaissance. Phase I is a rapid assessment of the airfield after an attack to get a general idea of the damage and to locate possible areas for surveying. This phase is usually conducted by observation posts, video

feeds, or imagery captured devices. Phase II is the process of precise measurements and reporting of damage so that data can be used to generate courses of action to restore the airfield. Phase II is performed with personnel on the ground doing physical measurements to get better accuracy of damage.

1. Importance and Necessity for ADA and ADR

To provide aviation power projection for U.S. Military forces, ADA and ADR are essential operations to restore airfields that have been damaged. Failure to restore airfields can hinder air operations, which can affect other military operations that may need their support. According to the air force pamphlet (AFPAM) 10-219, *Airfield Damage Repair Operations*, "Airbases can be the most immediate and lucrative targets for an adversary, because it is far more effective to destroy aircraft while they are on the ground than to hunt them in the air. Destroy the infrastructure that supports the aircraft, and you essentially destroy air operations. Not only must the United States maintain the capability to recover our own airbase after an enemy attack but must also capable of restoring an enemy airfield after US seizure" (DAF, 2012, p. 9). The U.S. military forces must project airpower in various amounts and restrictive regions and territories in the world. Since the U.S. forces are operating in remote airfields, there is a need for ADR to ensure that air operations do not get stalled. ADR is a vital function and "provides commanders with the ability to restore air operations at bases to ensure the timely and effective employment and sustainment of US airpower in support of America's global interest" (DAF, 2012, p. 11).

B. CURRENT STANDARD OPERATING PROCEDURES

The overall concept for ADA and ADR is presented in the AFPAM 10-219 for the United States Air Force (USAF) and in the Marine Corps Warfighting Publication (MCWP) 3-21.1 for the United States Marine Corps (USMC). The doctrines highlight the command structure and organization for both services and the procedures for executing the ADA and ADR mission.

1. Organization United States Air Force

For the USAF the Emergency Operations Center (EOC) implements and directs all base recovery forces and operations including ADR (DAF, 2012). The EOC determines and tracks base damage and uses data to develop a recovery strategy that is approved by the Installation Control Center (ICC). The EOC "determines impact on the base mission and maintains the status of personnel, casualties, and material resources" (DAF, 2012, p. 26). Once recovery strategy has been approved, the EOC directs the recovery actions and tracks progress. For ADA, the EOC tracks the damage and UXO data transmitted by the ADATs. Information collected assists leaders in determining three minimum operating strip (MOS) candidates, which are the areas of the airfield that can be used to launch and recover aircraft (DAF, 2012). The ICC chooses and approves the MOS that are viewed most beneficial for air operations, which the EOC then oversees ADR operations and UXO safing (DAF, 2012).

The airfield damage assessment teams "determine and report the location, types, and numbers of UXO, and the location, types, and quantity of airfield pavement damage to the EOC" (DAF, 2012, p. 47). Due to the size of an airfield, there are usually at least three ADATs required to do the assessment. The team consists of an EOD technician, engineer specialist, and one or more augmentees (DAF, 2012).

The MOS selection team receives damage and UXO information from the ADATs and then identifies usable and acceptable MOS. The goal "is to locate the best available MOS that can be repaired in the least amount of time" (DAF, 2012). The team is comprised of an engineer technician who plots data received from ADATs and another team member who operates the radio and records data.

2. Organization United States Marine Corps

In the U.S. Marine Corps, the Marine Wing Support Squadron (MWSS) maintains and operates the Aviation Ground Support Operation Center (AGSOC) responsible for the base recovery and ADR, which are part of the Base Recovery After Attack (BRAAT) procedures (USMC, 2016). BRAAT is the air base plan for restoring the operations and mission capabilities after an enemy attack. The AGSOC responsibilities include

developing the recovery plan for the airfield that is approved by the airfield commander, directing the recovery process and monitoring the recovery progress, and directing the teams and personnel involved with the recovery process to include the damage assessment teams (DATs); damage assessment and response teams (DARTs); aircraft rescue and fire-fighting; EOD; Nuclear, Biological, and Chemical (NBC) defense and decontamination teams; roving controller; and Rapid Runway Repair (RRR) officer in charge (OIC) (USMC, 2016).

Similar to the USAF ADAT, the damage assessment team patrols and surveys for airfield damage searching for "craters, spalls, and UXO on the runways, taxiways, and facilities that directly support aircraft operations" (USMC, 2016, p. 69). The DATs report all damage and UXO location to the AGSOC. The number of DATs required for ADA can range from two to four depending on the size of the airfield. The DAT consists of a team leader, two EOD technicians, radio operator, spall damage accessor, and two 1371 combat engineers for crater assessment (USMC, 2016).

Same as the USAF MOS selection team, the USMC MOS selection team is located in the AGSOC where it receives the airfield damage reports to determine usable areas of the runway to launch and recover aircraft. The MOS selection team estimates the time required to repair damage and remove UXO for a potential MOS, which is then presented to the commander for approval.

3. Airfield Damage Assessment Process

The purpose of ADA is to locate and measure spalls, craters, and camouflets and to locate any UXO. As mentioned before, ADA is split into two phases: Phase I initial reconnaissance and Phase II detailed reconnaissance. ADA is crucial because the information provides the MOS selection teams in selecting an MOS and the engineers in planning to conduct ADR. Table 1 shows the types of damages that are being searched and assessed during the ADA process.

a. Phase I: Initial Reconnaissance

The purpose of this phase "is to rapidly assess the attack recovery environment by identifying broad areas where airfield pavement was damaged" (DAF, 2016, p. 11). The assessments are done at a distance from observation posts, camera feeds, UAVs, aircraft or other devices that provide images of the airfield in order to report estimation of the size and location of damage and possible UXO. Marker systems are sometimes laid out on the runway to provide referencing to the location of an airfield at 50 to 100 foot intervals (DAF, 2012). If personnel can see the marker in relation to the damage, then they can accurately assess the location within 100 feet (DAF, 2012). The assessments are not expected to be precise due to the distance that the observations are being made, but the information will provide ADATs a general area for searching and start the process for selecting an MOS (DAF, 2016).

Table 1. Airfield damage types.

Type of Damage	Description	Image
Spall	Spalls are damages to the runway that are less than 5 feet in diameter that do not penetrate the runway base course and subgrade (USMC, 2015).	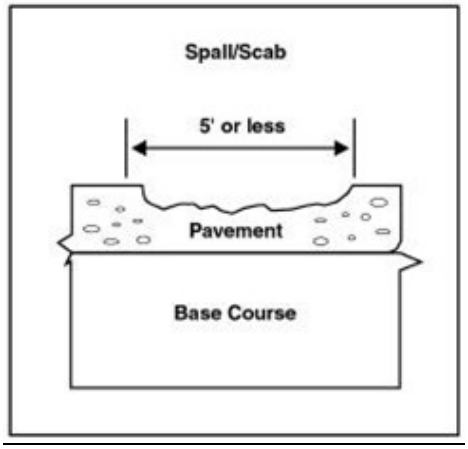

Type of Damage	Description	Image
Small Crater	Small craters are less than 20 feet in diameter and will penetrate the pavement, base course, and possibly the subgrade of the runway, but usually will not cause pavement upheaval (DAF, 2016).	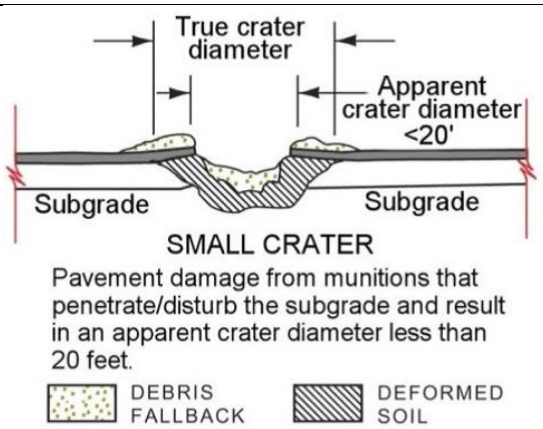
Large Crater	Large craters are 20 feet or more in diameter and will penetrate the pavement, base course, and subgrade and will cause pavement upheaval (DAF, 2016).	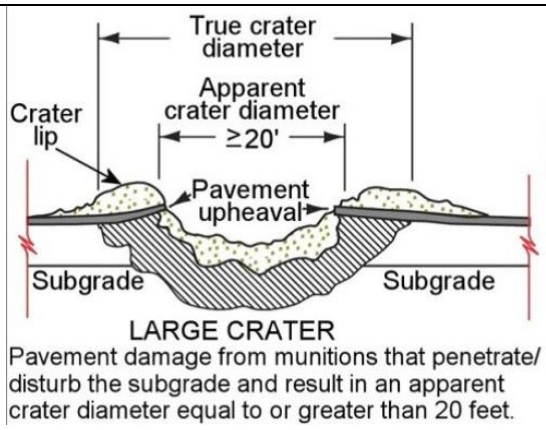
Camouflet	Camouflets are deep penetrating but small diameter craters usually caused by penetration projectiles with a time-delay fuse (USMC, 2015).	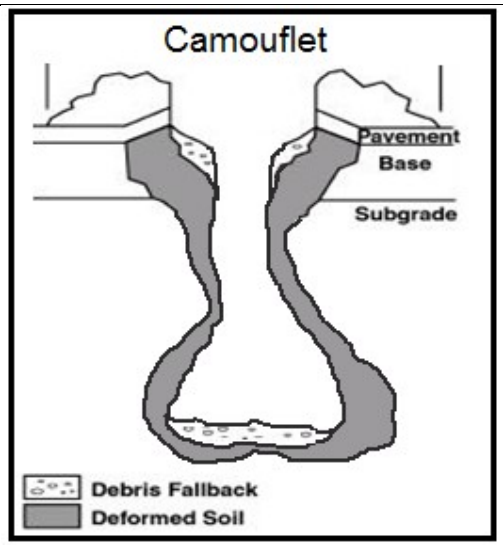

Type of Damage	Description	Image
UXO	UXO are explosive weapons that did not explode when they were employed and still pose a risk of detonation.	

Adapted from USMC (2015); DAF (2016); Hamilton, (2012).

b. Phase II: Detailed Reconnaissance

Phase II requires precise measurements and reporting of damage to the EOC and MOS selection team so that the data can be used to form the different courses of action for the MOS selection and restoring the airfield operations (DAF, 2016). Depending on the amount of damage, at least three or more ADATs are deployed on predetermined travel routes or routes that have been modified due to the results from Phase I reporting. Damages done to the takeoff and landing runways and the primary taxiways are priority in the reconnaissance so that information can be reported to the operations center for damage plotting and MOS selection. Figure 1 simulates a possible damage assessment on part of the runway demonstrating the scenarios that assessment teams can experience. The two different methods in conducting the detailed reconnaissance with ground personnel are mounted and dismounted.

In mounted reconnaissance, vehicles are used to conduct the assessment which provides speed and protection to the ADATs. Armored vehicles are ideally used to provide protection to the ADATs from possible UXO detonation while the team is conducting the assessment. Though vehicles are a faster method of doing ADA, there is a loss of visibility while in a vehicle which can cause errors to measurements of damage or loss of awareness in identifying UXO (DAF, 2016). Depending on the efficiency and experience of the

ADAT, damage assessment can be done visually without manual measurements and estimates of damage within 100 feet distance to be acceptable (DAF, 2016).

In the dismounted method, teams conduct surveys of the taxiways and runways on foot which can be slow and hazardous but provides more accuracy in the damage assessment. ADATs walk specified routes that have been assigned to the team to classify and pinpoint damages. During assessments, ADATs make measurements of damage by visual estimation or pacing in order to get the dimensions of craters or to determine the features of a UXO. In order to provide the location of damage, teams use GPS or airfield markings to relay the information to the EOC or AGSOC (DAF, 2012). To walk the runway and taxiways on foot is very time consuming due to the size of the airfield and ADAT members are more exposed to UXO and blast hazards (DAF, 2012).

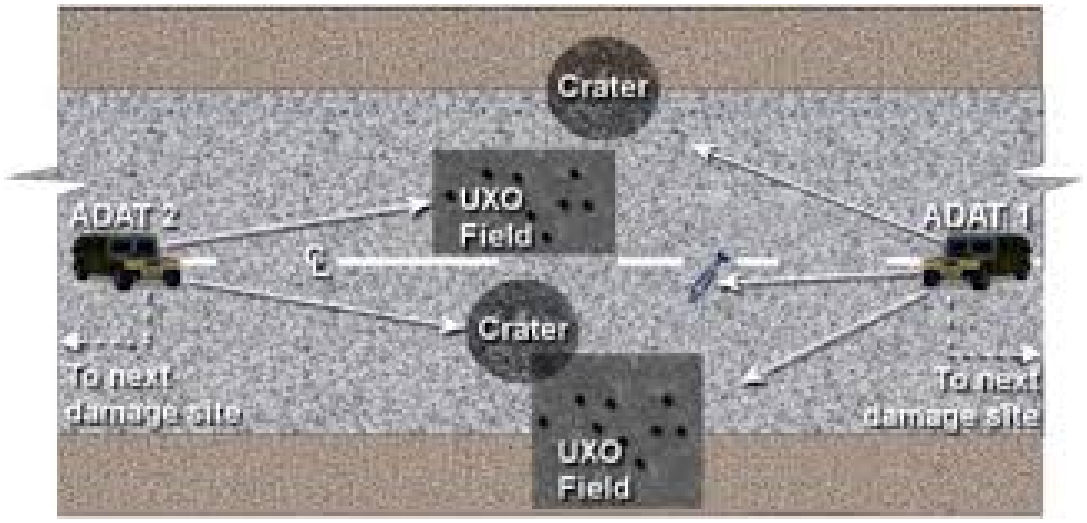

Figure 1. Multiple damage and UXO assessment. Source: DAF (2016).

During the damage assessment, the ADATs gather damage information containing the damage type, location of damage, size, and the number of damage types as well as locate, classify, and report all UXO to the operations center. Information about UXO includes “location, quantity, size, shape, color, distinctive markings, and fuze type and condition” which is important to provide to the operations center because all located UXO “within 300 feet of repair operations or aircraft operating surfaces must be reported due to

the possibility of UXO detonating, which could cause damage to surfaces, personnel, or equipment" (DAF, 2016, p. 21). When conducting damage assessments, the airbase determines priorities of search so that travel routes are premade for the ADATs. The airbase search priorities set forth by the AFTTP 3-32.11 can be seen in Table 2.

Table 2. Assessment priorities. Source: DAF (2016).

Priority	Airfield Location
1	Takeoff and Landing Surfaces (i.e. runways, alternate launch and recovery surfaces, and taxiway segments long enough to permit aircraft launch and recovery)
2	Access pavements to takeoff and landing surfaces
3	Aircraft parking areas
4	Infrastructure such as lighting (including Precision Approach Path Indicators [PAPIs], utility lines, signage, etc.)
5	Aircraft arresting systems
6	Aircraft rearming and refueling areas
7	Other specified locations as defined in the Facility Prioritization List or as determined by installation leadership

An example of damage plotting and potential MOSs can be seen in Figure 2, which provides a picture for the ICC to make a decision for recovery operations. The MOS is the airfield surface that require the least amount of time to repair but also provide a suitable launch and recovery surface for the appropriate aircraft. When selecting an MOS, different aircraft platforms will require different MOSs and also operational requirements will need to be considered (DAF, 2012). When the MOS has been selected, EOD teams are employed to render-safe and remove all UXO that pose a potential threat to the selected MOS and to the ADR activities. ADR, which includes crater and spall repair, is conducted in conjunction either with or immediately following EOD activities so that the selected MOS and supporting airfield surfaces can be restored for aviation operations to be continued.

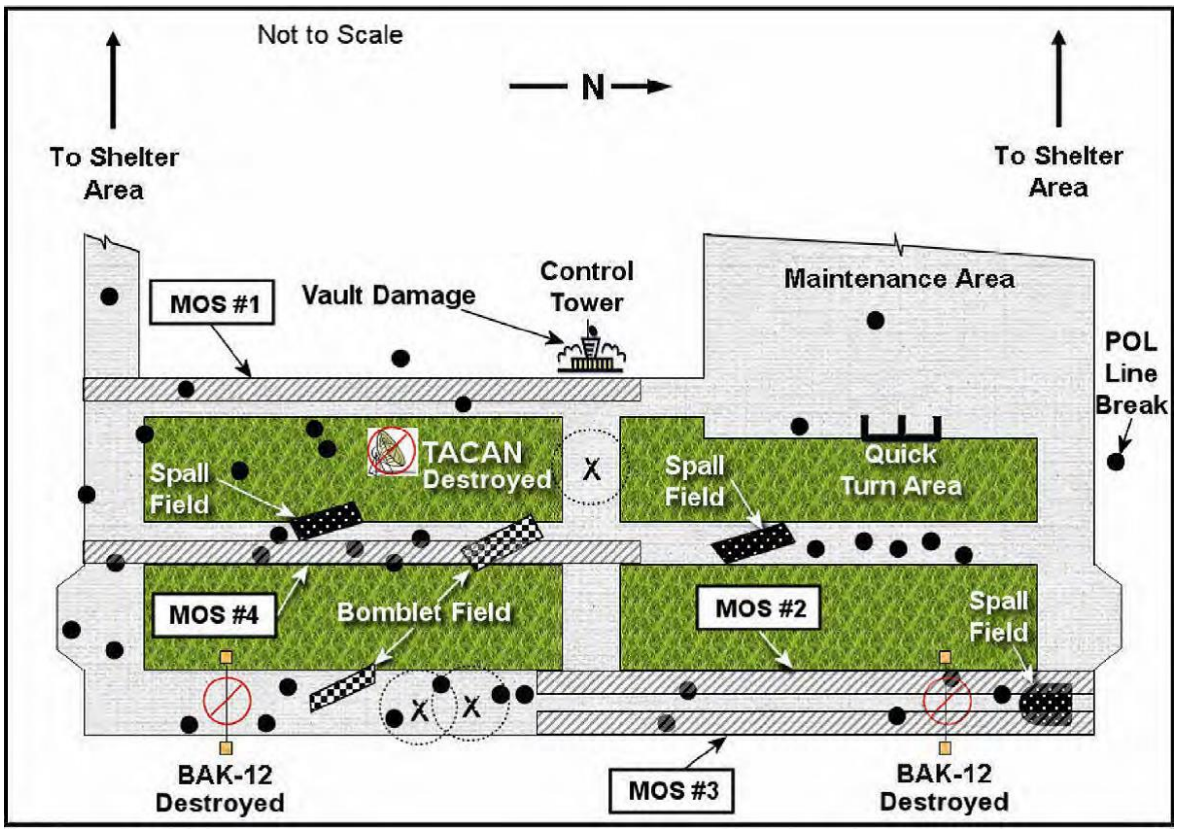

Figure 2. Runway damage listing and potential MOS. Source: DAF (2012).

c. Disadvantages to Current SOPs

The current ADA and ADR process has some disadvantages including time consumed, hazards to ground personnel, and inaccuracies due to transmission of information. The purpose of ADR is to "provide the installation commander with capabilities to sustain and restore flying operations rapidly after enemy attack" (DAF, 2012, p. 12). Though the purpose of ADR is to rapidly restore operations, the current process is very time consuming and with today's environment and threats the process needs to be even quicker. Typical runway lengths are 2,000, 2500, 3,000, 6,000, and 10,000 feet long for military operations (DAF, 2012). The long runways require more time for ADATs to conduct damage assessment and depending on the size of the airfield and the damage sustained, ADA can possibly take up multiple hours to complete not including the time to assemble the ADATs and employ them. This time to complete ADA affects the completion time of ADR specifically the removal of UXO and repair of craters and spalls. The U.S.

Air Force has different requirement times to accomplish repairs to damaged airfields. Depending on the equipment sets and engineer personnel available, the U.S. Air Force has a requirement to complete repairs of one crater in four hours with the basic equipment set or two craters in four hours with the heavier package set (DAF, 2012). Also, the U.S. Air Force has a requirement of four hours to repair up 400 spalls. These different requirement times do not include the time to remove UXO and any additional damages done to the MOS (DAF, 2012).

As mentioned earlier, detailed reconnaissance in Phase II is done via mounted or dismounted. The environment after a base attack is hazardous and poses risks to the ADATs who are conducting ADA. Whether ADATs are in vehicles or walking their routes, UXO and possible enemy actions can make ground personnel vulnerable and potential to have casualties. If an ADAT sustains casualties, then the ADA process will be stalled until another team can be employed to take over the route.

During Phase II, there is a possibility for communication inaccuracies and confusion from the ADATs and other ground personnel during ADA. The communication process for ADA has EOD and the base engineers using different radio nets to transmit information. Since the EOD and engineer representative of each ADAT will transmit information to the EOC separately then there is a potential for redundancy of information and confusion (DAF, 2012). Also, with many teams on the ground, there is potential of high transmission traffic or possible interruption of communications causing inaccuracies of information and confusion within the EOC.

C. TECHNOLOGIES USED FOR ADA

Technologies have been explored and developed to assist and improve ADA and ADR. This section discusses some of the technologies that have been used or currently being research for ADA operations.

1. iFerret and Super Bullseye

The USAF experimented with Stratech Systems products the iFerret and Super Bullseye systems for testing and evaluating technologies that could be used for the Air

Force's Rapid Airfield Damage Assessment System (RADAS) (Stratech Systems Limited, n.d.). The iFerret is a static high resolution camera system placed on a tower that was originally designed to detect foreign object debris (FOD) on an airport runway or taxiways (Stratech Systems Limited, n.d.). Figure 3 is image of the iFerret system. The iFerret system can be installed at multiple locations along the flight line and taxiways in order to locate and categorize damages done on the runway after an enemy attack. The Super Bullseye is weapons scoring system software that "automatically detect and score impacts of missiles, rockets, bombs and small rounds with high precision, locating all visible weapon impacts to an accuracy of one meter" (Stratech Systems Limited, n.d.). The combination of the iFerret and Super Bullseye provided an automatic detection system for airfield damage but has been discontinued due to infrastructure and operational requirements (Clark, 2018).

Figure 3. iFerret static position camera. Source: Stratech Systems Limited (n.d.).

2. Geospatial Expeditionary Planning Tool

Geospatial Expeditionary Planning Tool (GeoExPT)

> is a decision support tool for mission planners and engineers to provide the means to create geospatially accurate base layout plans, meet beddown requirements, automate aircraft parking, and analyze and repair airfield damage for optimal selection of the Minimum Airfield Operating Surface (MAOS) in accordance with Department of Defense (DoD) standards. (United States Government [USG], 2018)

GeoExPT is used with Autodesk's AutoCAD Map 3D software, which provides geospatial map representation of an installation (USG, 2018). Figure 4 demonstrates how GeoExPT is used to establish the airfield providing the commander and staff the ability to organize and visualize the installation. One of the functionalities for GeoExPT is specifically for ADR activities in order to centralize recovery operations through organization and management tools. GeoExPT provides features to plot and manage damage on an airfield including the damage type such as crater, spall, camouflet, and UXO. Figure 5 is an image of GeoExPT being used to plot damage specifying the type, location, and amount. With the damage plotted, GeoExPT can determine and assist with the selection the MOS candidates in order to expedite the recovery operations for the airfield.

Figure 4. GeoExPT damage plotting feature. Source: USG (2018).

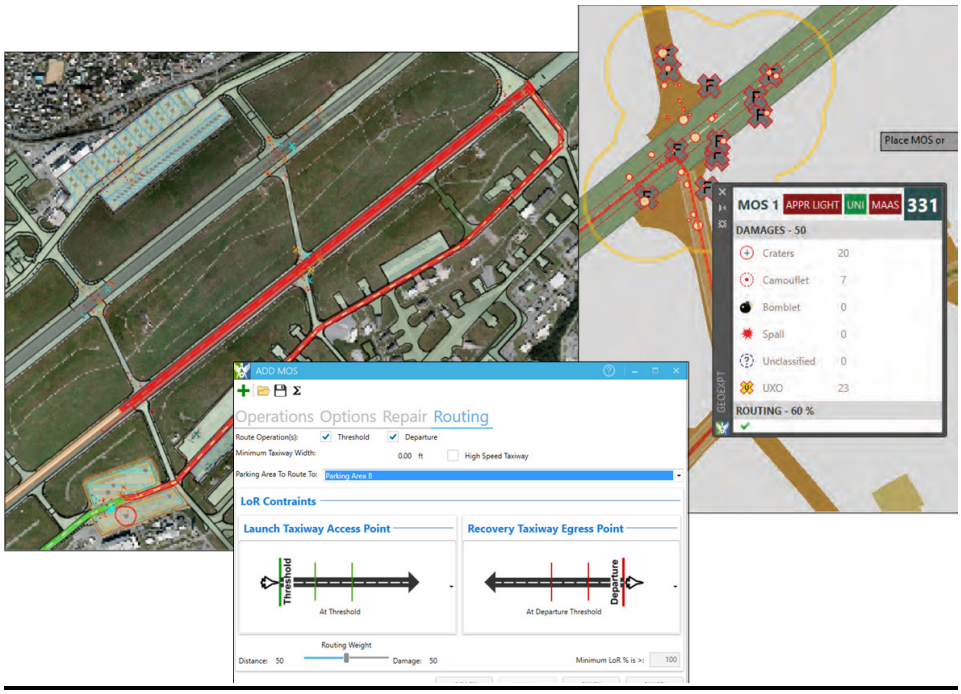

Figure 5. GeoExPT MOS selection feature. Source: USG (2018).

3. Previous Work at NPS

Previous research has been done at NPS to assist in the improvement of ADA specifically research in using drones with a high resolution camera by LT Nicholas Davis, USN, and drones with a Light Detection and Ranging (LIDAR) camera by Capt Eric McNeely, USMC. LT Davis focused on using cheap and readily available COTS unmanned aerial vehicles (UAV) with a high resolution camera to survey and capture damage data on a runway. The UAV used for this research was the Phantom 4 Pro UAV, which has a maximum flight time of 30 minutes with a range of 7 km that connected to an iPad Pro10.5 with Wi-Fi and cellular capabilities for controlling the drone (Davis, 2018). To conduct waypoint mapping and to collect data along the flight route, Pix4DCapture mobile application software was installed. This software plans the optimal flight path within a designated area for the UAV to do automatic flying and image capturing (Davis, 2018). The drone would conduct an initial runway scan and a second scan for damage localization. The initial scan was done to provide critical and timely information of possible runway damages so that MOS selection teams can start recording data for its MOS

selection and ADR teams can prepare for repair estimations (Davis, 2018). The second runway scan is used to get a more detailed mapping of the damage that has been identified for repair operations using 3D model programs. LT Davis's work identified positive impacts of ADA improvement using the UAV and surveying programs (Davis, 2018, p. 71). The low cost equipment and autonomous surveying process decreased the time of surveying airfield damage and increased assessment accuracy to support ADA.

Capt Eric McNeely conducted research on LiDAR systems that are attached to UAVs in order to get a thorough assessment of the actual damage including the diameter and the depth. This detailed data provides an accurate picture of the damage sustained which allows personnel to calculate materials for repairing damage. The COTS UAV used for testing was the DJI Matrice 600 which has flight time of roughly 36 minutes and a maximum range of 3.1 miles (McNeely, 2018). Attached to the drone was the LiDAR Garmin Lite v3 and an Adafruit Ultimate GPS module. LiDAR can determine the distance or depth of an object by calculating the time delay that light emitted from the LiDAR system to the object and back (McNeely, 2018). In order to calculate the diameter of damage, the GPS module was used by measuring the start and end latitude and longitude coordinates of damage. These coordinates were then used in the Haversine Formula which calculates the distance between two points through longitude and latitude differences (McNeely, 2018). With these two systems attached to the UAV, the drone during experimentation simulated two flyovers. The first flyover was an initial scan to identify damage with the GPS module and outline the shape of the damage with the LiDAR (McNeely, 2018). The second flyover scanned the depth of the crater or spall with the LiDAR which can assist with repair estimations for the engineers of the airfield. The system that Capt McNeely developed was successful in identifying and accurately measuring damages in a realistic environment with a low cost and low power system of design.

D. MICROELECTROMECHANICAL SENSORS

MEMS technology is "used to create tiny integrated devices or systems that combine mechanical and electrical components. MEMS devices can range in size from micrometers to millimeters and can detect changes in the environment on the micro scale and process the information" (PRIME Faraday Partnership, 2012, p. 1). PRIME Faraday Partnerships informs that "While device electronics are fabricated using 'computer chip' IC technology, the micromechanical components are fabricated by sophisticated manipulations of silicon and other substrates using micromachining processes. Processes such as bulk and surface micromachining, as well as high-aspect-ratio micromachining (HARM) selectively remove parts of the silicon or add additional structural layers to form mechanical and electromechanical components" (PRIME Faraday Partnership, 2012, p. 2). MEMS devices typically consists of microsensors, microelectronics, and microactuators integrated on a silicon chip. Microsensors measure changes in the information of the environment specifically mechanical, thermal, magnetic, chemical, or electromagnetic properties (PRIME, 2012). MEMS technology has become very popular since it has reduced the size of many types of sensors at lower cost while improving performance. Such sensors include acoustic sensors that detect and locate sound sources, among them, gunshots or bomb explosions to a very accurate degree (Wilmott, 2015).

E. SMALL MICROCONTROLLER DEVICES

The Arduino is a microcontroller board that can execute code using simplified version of C++ language to collect data from a wide aspect of sensors to include acoustics (Arduino, 2018). The Arduino is a circuit board that can be programmed using Arduino Integrated Development Environment (IDE) software write and upload code on the board for different applications. Arduino products come with imbedded or downloadable software support libraries, which provide extra functionality for design and application (Arduino, 2018). The Arduino Uno components include 20 input and output pins, 16 MHz resonator, a USB connection, and a power jack that can operate on an external supply from 6 to 20 volts with 20 to 40 mA of operating current (Arduino, 2018). The Arduino Uno memory consists of the ATmega328 which has 32 KB of memory, 2 KB of SRAM, and 1

KB of EEPROM (Arduino, 2018). The Arduino Nano is a compact version of the Uno with the only difference is that the Arduino Nano has two more digital input and output pins compared with the Arduino Uno. Figures 6 and 7 are images of the Arduino Uno Rev3 and Arduino Nano, respectively. The Arduino is highly customizable microcontroller that can receive and process data into readable information at a low cost and low power making it ideal for small device applications.

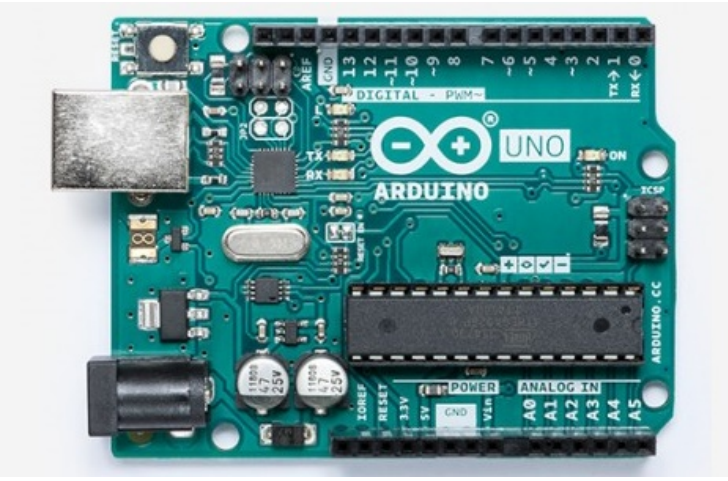

Figure 6. Arduino Uno Rev3. Source: Arduino (2018).

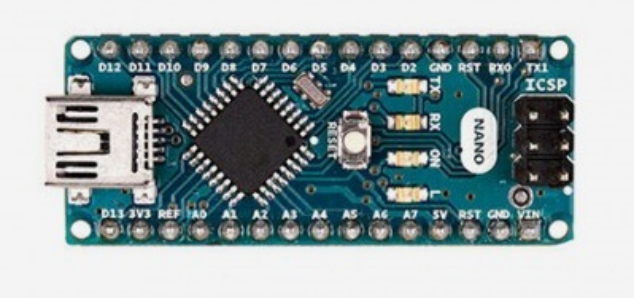

Figure 7. Arduino Nano. Source: Arduino (2018).

F. SUMMARY

This chapter has provided an overview of the ADA process and how it affects the ADR procedures and the restoration of an airfield once it has come under attack by an enemy. U.S. military forces operate around the world and must be able to project airpower

in remote locations and on foreign soil. ADR is a critical function to airfield and flight operations and the current process for conducting ADA is effective but can be improved through incorporation of technology. The current ADA process is time consuming and hazardous to the ADATs who are surveying the damage on the airfield during phase II. By incorporating an acoustic ground sensor network composed of MEMS Direction Finding sensors, will help assist in the detection and location of bomb impacts on the airfield. This sensor network could accelerate the ADA process by providing locations of known bomb impacts so that surveying of the damage can be done quicker by ADATs. The next chapter describes the system design and set up of the acoustic ground sensor network to improve the ADA process.

III. HARDWARE SELECTION AND SYSTEM DESIGN

This chapter discusses the acoustic ground sensor network for ADA including the description of the main components and equipment, circuit design, software applications, and algorithms. The first section describes the system architecture. The subsequent section details system components, including the MEMS direction finding (DF) sensor, communication module, GPS module, and microcontroller. This chapter concludes by discussing the algorithms and flow process to visualize and present that data collected.

A. SYSTEM ARCHITECTURE OVERVIEW AND GOAL

The main purpose of this research is to design a network of acoustic sensors that can detect and triangulate bomb impacts on an airfield in order to support the ADA process. Triangulating bomb impacts during a base attack rapidly provides precise and accurate locations of damage as part of Phase I, initial reconnaissance of ADA. Since damage locations would have already been identified by the sensor network, it will assist the process of Phase II, detailed reconnaissance by helping to reduce the number of ADATs required to verify the damage and to decrease the assessment time. The sensor nodes can be arranged in specific locations on the airfield or air base to maximize coverage for detection and localization. The network of sensors will transmit data to a planning tool interface that the personnel can use to determine further damage assessment in Phase II and recovery operations.

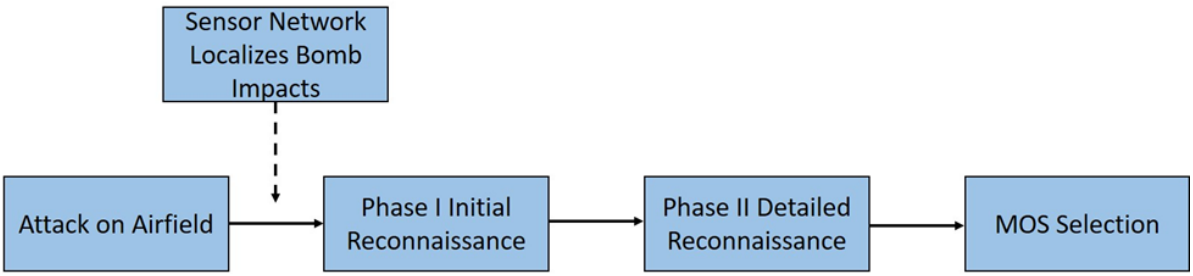

Figure 8. Sensor network implementation during ADA

Figure 8 shows where the ground sensor network fits in the flow of the ADA process. It activates when the base comes under attack so that there is autonomous and instantaneous data being collected and processed while personnel are sheltering in place. With the data, recovery personnel have a general idea of location of the damage sustained which is mapped on a display.

Our goal is to build a low cost and easily deployable sensor network that can produce accurate results to support ADA. The sensor network needs to be able to operate in an active environment that can wirelessly process and transmit data without pulling data services from the military communication components. Also, the sensors need to be small that they will not affect military operations, and they should require low power and maintenance in order reduce manpower requirements and improve sustainability. Each sensor node is comprised of a MEMS DF Sensor, a nRF24L01+ transceiver module, NEO-6M GPS Module, and an Arduino Uno Rev3 while a hub receiver will be comprised of a nRF24L01+ transceiver module, and an Arduino Uno Rev3, which will be discussed in the next section.

B. SYSTEM COMPONENTS

This section goes into detail about the main components for the ground acoustic sensor network comprised with the MEMS DF Acoustic Sensor, nRF24L01+ transceiver module, NEO-6M GPS Module, and an Arduino Uno / Nano.

1. MEMS Direction Finding Acoustic Sensor

The main component of the sensor node is the MEMS DF acoustic sensor that was researched and designed by Dr. Gamani Karunasiri and Dr. Fabio Alves, Department of Physics, Naval Postgraduate School (U.S. Patent No. 9843858B1, 2017).

a. The Ormia Ochracea

The MEMS DF acoustic sensor is bio-inspired, emulating the hearing system of the *Ormia ochracea* fly, which has a hearing organ that can detect the direction of a chirping cricket with an accuracy of less than two degrees (Wilmott, 2015). The parasitic fly has two eardrums that are separated by a cartilaginous bridge about 0.5 mm wide which allows

the fly to detect wavelengths about 50 times greater, for the purpose of laying eggs in the chirping cricket (Karunasiri, Swan, & Alves, 2017).

Research done by Ronald Miles, Daniel Robert, and Ron Hoy on the *Ormia ochracea's* eardrum mechanical structure explains that animals localize sound sources by detecting the minute difference in sound intensity and time arrival between both ears: "In relatively large animals where the distance between the ears is substantial relative to the wavelength of sound, interaural time, and intensity differences are large enough to be detectable by the central nervous system" (1996, p. 3059). Animals such as humans can successfully detect a sound source if the sound wavelength is similar or greater than the separation size of the two eardrums. Unlike animals with large eardrum separation, the *Ormia ochracea* has two tympanal membranes that are connected by a flexible mechanical lever about 0.5 mm wide. The tympanum organ system provides a highly effective sound localization since "mechanical coupling between the tympana acts to increase the time delay for the effect of sound travel…the mechanical system also produces significant interaural level differences which will also greatly facilitate the neural processing of directional information" (Miles et al., 1996, p. 3060). Miles et al. (1996) transferred their data into a mechanical simulation of the *Ormia ochracea* tympanal membrane using dual cantilever to represent the dynamical properties in Figure 9. Figure 9 represents the design of the MEMS DF acoustic sensor.

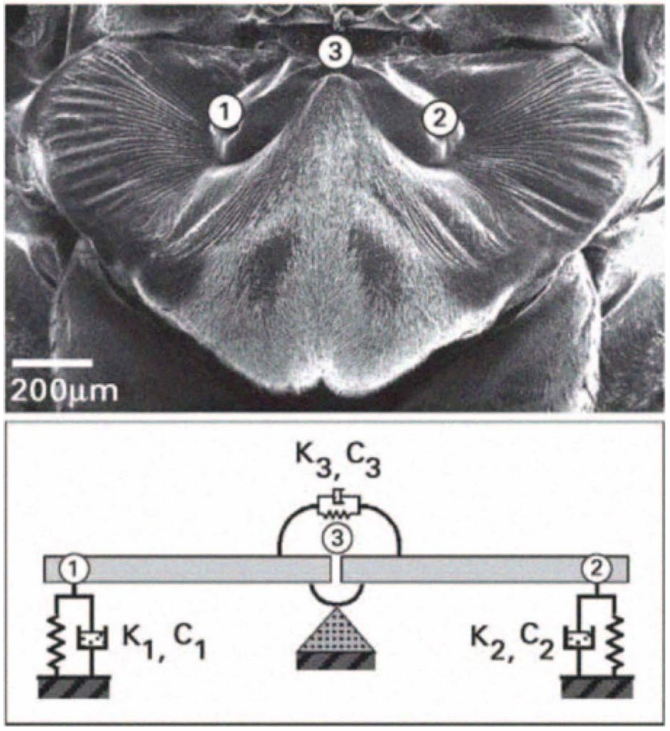

Figure 9. Mechanical model simulating the *Ormia ochracea* ear organs. Source: Miles et al. (1996).

The two eardrums of the fly also have two natural resonant frequencies that have two modes of oscillation: a rocking mode and bending mode (Miles et al., 1996). The rocking mode is when the ears move out of phase with each other which is caused by pressure differences on each ear. Figure 10 part (b) shows an example of the rocking mode in relation to the mechanical structure of the fly's ear drums. The bending mode demonstrates when the ear drums are moving in phase, which is the result of the sum of all forces on the ear drums (Miles et al., 1996). Figure 10 part (b) also represents the bending mode of the mechanical structure in relation to that of the fly's eardrums. The resonant modes increase the directional sensitivity by magnifying the oscillation phase and amplitude differences between the ear drums (Miles et al., 1996).

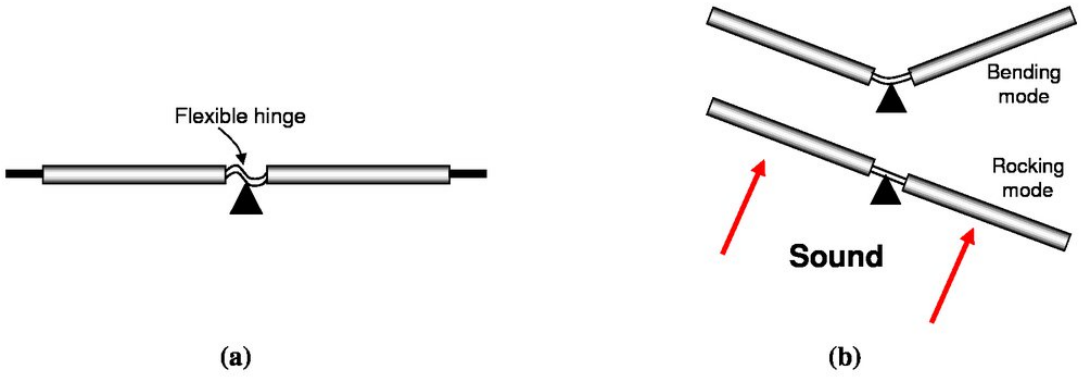

Figure 10. Schematic of (a) mechanical structure of fly's eardrums and (b) vibration modes under sound excitation. Source: Karunasiri et al. (2017).

b. MEMS Sensor Design

The *Ormia ochracea* ear drum structure have inspired the design of sound localization sensors using MEMS technology. The sensor designed by Dr. Gamani Karunasiri and Dr. Fabio Alves operates at a resonance frequency of a mechanical system vice what the conventional broadband microphones use an off resonance detection (Karunasiri et al., 2017). The sensor is fabricated on a silicon-on-insulator (SOI) substrate which provides a device layer thickness of about 25 µm. The sensor used for this work "consists of two 1.5 mm x 1.6 mm wings connected in the middle by a 2.7 mm x 30 µm bridge. The entire structure is connected to the substrate by two torsional legs at the center. The frequency response of the sensor showed two resonance frequencies at approximately 1.1 kHz (rocking) and 1.5 kHz (bending)" (Karunasiri et al., 2017, p. 3). The bending resonance of 1.5 kHz is determined to be the operating resonance for the sensor which is used for measurement of directional responses (Karunasiri et al., 2017). Figure 11 part (b) is an optical micrograph of the fabricated sensor and its dimensions. Figure 11 part (a) illustrates the bending and rocking modes of the oscillations during simulated displacements.

The design of the sensors also includes comb finger capacitors, which are integrated in the edges of the wings as shown in Figure 11 part (c) (Wilmott et al., 2016). This feature allows for electronic readouts to convert mechanical oscillations due to acoustic

stimulation into useful electric signals. A reference capacitor, seen in Figure 11 part (b) label (4), was fabricated next to the sensor to allow the measurement of differential capcitance of the comb fingers using a MS3100 chip from the Irvine Sensors (Wilmott et al., 2016). The comb fingers are misaligned vertically to that of the substrate due to the residual stress after fabrication (Karunasiri & Downey, 2014). The MS3100 measures the capacitance change from the comb fingers and produces an electrical voltage output that is used to determine an incident angle of direction (Karunasiri et al., 2017).

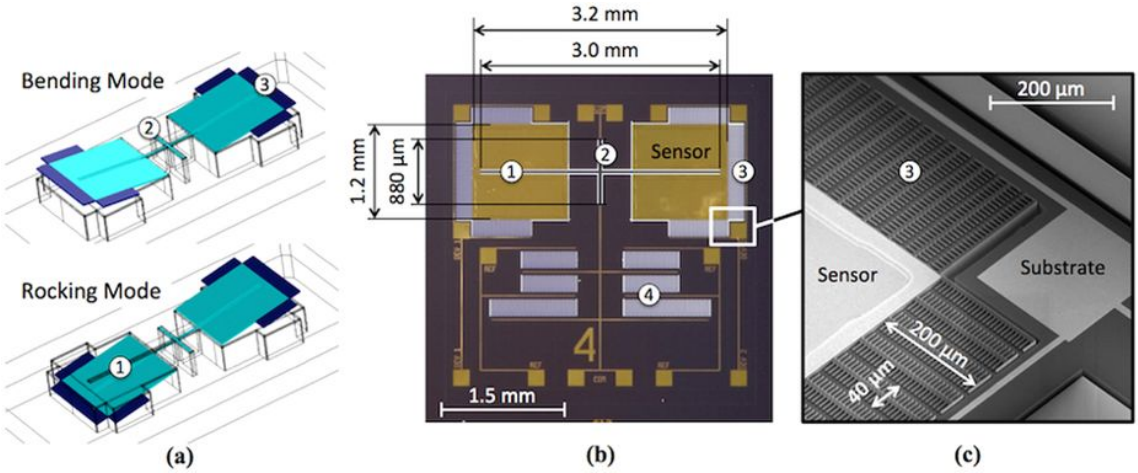

(a) Bending and rocking modes of sensor during oscillation displacement. (b) Optical micrograph showing the two wings (1) connected by the bridge, torsional legs that connect the freestanding sensor to the substrate (2), comb fingers (3), and the reference capacitor (4) (Wilmott et al., 2016).

Figure 11. Layout of MEMS directional acoustic sensor. Source: Wilmott et al. (2016).

c. Dual Sensor

To remove directional ambiguities and improve the directional responses to the system, two sensors are arranged at a canted angle θ_{off} which provides an effective coverage of incoming sound. The goal of the angle is to have the incident sound interact with the left sensor at $\theta - \theta_{off}$ and the right sensor at $\theta + \theta_{off}$ in order to provide an effective coverage of $-90° + \theta_{off}\ to + 90° - \theta_{off}$ (Wilmott et al., 2016). Figure 12 shows the arrangement of two sensors canted at the angle θ_{off}. From this particular arrangement, Equation (1) calculates the voltage for the left and right sensor (Wilmott et

al., 2016). The sound pressure on each sensor is considered equal due to the proximity of the two sensors and is incorporated into the Equation (1) as P_o. The calibration constants α_L and α_R are a "proportionality constant that depends on the parameters of the readout circuit" (Wilmott et al., 2016, p. 3). The calibration constants come from output of each sensor when keeping the sound pressure and incident angle the same in order to account for any mismatch between the sensors (Wilmott et al., 2016).

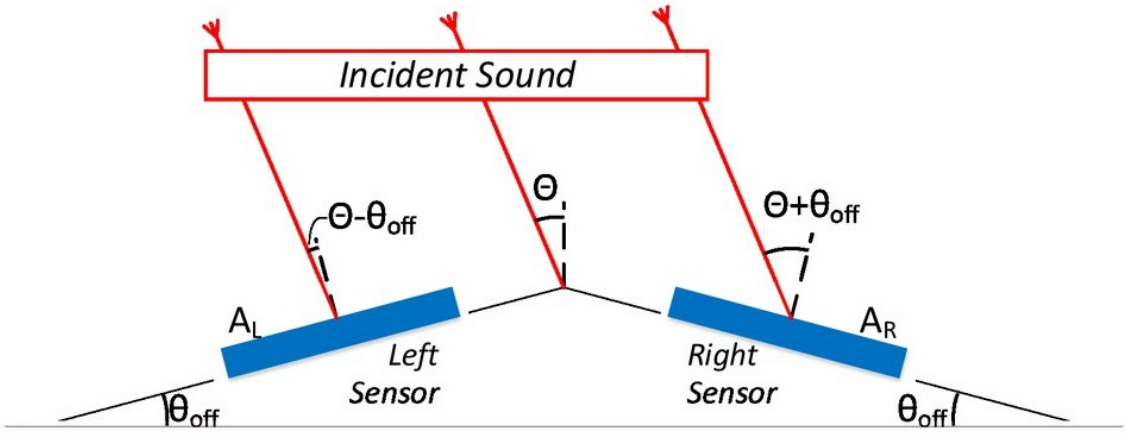

Figure 12. Arrangement of two MEMS DF sensors canted at θ_{off}.
Source: Wilmott et al. (2016).

$$V_L = \alpha_L P_o \cos(\theta - \theta_{off}) \text{ and } V_R = \alpha_R P_o \cos(\theta + \theta_{off})$$
$$\text{for } -90^\circ + \theta_{off} \leq \theta \leq 90^\circ - \theta_{off} \quad (1)$$

The unknown sound pressure amplitude can be disregarded since the values are considered equal when taking the ratio of the difference and sum of the left and right voltage signals in Equation (1) (Wilmott et al., 2016). The ratio of the two proportionalities can calculate the angle θ of the incident sound source, which is shown in Equation (2) (Wilmott et al., 2016).

$$\frac{V_L/\alpha_L - V_R/\alpha_R}{V_L/\alpha_L + V_R/\alpha_R} = \tan(\theta_{off})\tan(\theta)$$

$$\text{for } -90^{\circ} + \theta_{off} \leq \theta \leq 90^{\circ} - \theta_{off} \tag{2}$$

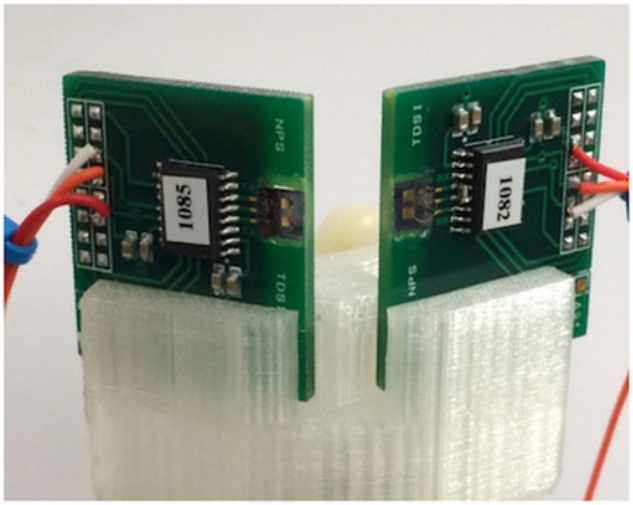

Figure 13. Dual sensor assembly. Source: Karunasiri et al. (2017).

Figure 13 shows the photograph of the dual sensor assembly with the 30° offset of the two sensors, similar to the assemblies used in this work. When tested, the sensor had a resonant response of 1.5 kHz for bending mode and produced an angular accuracy with 2° deviation between measured and actual angles (Karunasiri et al., 2017). The accuracy of the dual sensor setup for the MEMS DF acoustic sensor is suitable for use in this project to detect and localize bomb impacts on an airfield to support the ADA process.

2. RF Transceiver Module

To create a data network in the sensor system, nRF24L01+ transceiver modules, seen in Figure 14, designed by Nordic Semiconductor are attached to each sensor node and to the hub station where all data is collected. The size of the module board is 15.5mm x 40.7mm x 12.2 mm and the dimensions of the antenna are 87 mm x 9.5 mm (Nordic Semiconductor, 2008). The compact size module is capable of transmitting data over 800+

meters line of sight with a minimal power requirement and at the cost of $5.00 a module (Last Minute Engineers, n.d.-a). This inexpensive module provides the necessary and reliable transmission capability that is required for the design.

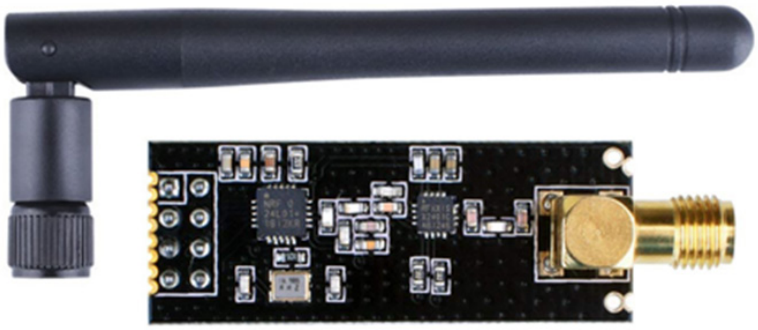

Figure 14. Nordic semiconductor nRF24L01+ transceiver module.
Source: Last Minute Engineers (n.d.-a).

a. Hardware Overview

The hardware of the nRF24L01+ transceiver modules consists of components that make the equipment ideal for the network aspect of the design.

1. Radio Frequency

The nRF24L01+ operates "on the world wide ISM band at frequencies from 2.400 GHZ to 2.525 GHz with the programming resolution of the RF channel frequency set to 1 MHz for 250 kbps and 1 Mbps data rate and 2 MHz for 2Mbps data rate to ensure there is no overlapping channels" (Nordic Semiconductor, 2008, p. 24). The module uses Gaussian frequency-shift keying (GFSK) modulation for data transmissions. GFSK is a form of frequency shift keying (FSK) which transmits a signal by either increasing or decreasing the frequency (Last Minute Engineers, n.d.-a). By increasing the carrier frequency for a specific duration represents a 1 symbol while decreasing the frequency for a specific duration correlates to a 0 symbol (Gerez, 2016). The main difference between FSK and GFSK is that a gaussian filter is applied to the signal in GFSK before creating the frequency modulation signal. The gaussian filter smooths the baseband signal which reduces the size

of the frequency bandwidth (Gerez, 2016). This narrower bandwidth reduces the possibility of interference with other channels during transmission. The nRF24L01+ channels use "a bandwidth of less than 1 MHz for 250 kbps and 1 Mbps and a 2 MHz bandwidth for 2 Mbps" (Nordic Semiconductor, 2008, p. 24). This gives the module 125 possible channels with 1MHz spacing depending on the selected data rate. Figure 15 shows the channel creation with the 1 MHz bandwidth.

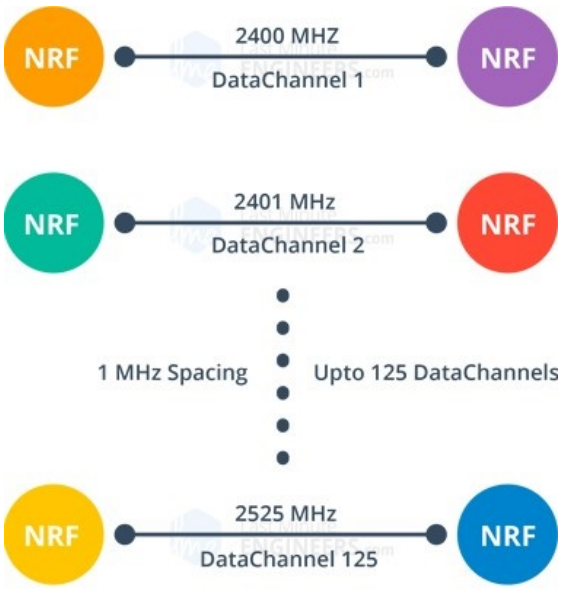

The transceiver uses the 2.4 GHz ISM band with each channel, using less than 1 MHz, which allows the module to create 125 different channels Nordic Semiconductor (2008).

Figure 15. nRF24L01+ frequency channel. Source: Last Minute Engineers (n.d.-a).

2. Power Consumption

The nRF24L01+ transceiver operates at a voltage of 1.9 to 3.6V, allowing the module to connect and function with an Arduino or any 5V logic microcontroller (Last Minute Engineers, n.d.-a). The transmission power for "the module supports programmable output power for 0 dBm, -6 dBm, -12 dBm or -18 dBm with an average current of 11.3 mA, 9.0 mA, 7.5 mA, and 7.0 mA respectively" (Nordic Semiconductor, 2008). During receive mode, the module has a current of 13.5 mA for 2 Mbps data rate, 13.1 mA for 1 Mbps data rate, and 12.6 mA for 250 kbps data rate (Nordic Semiconductor,

2008). During idle modes, the module consumes 900 nA in power down mode and 26 μA in standby mode (Nordic Semiconductor, 2008). Therefore, the average power consumption is 0.055 watts for the module.

3. SPI Interface

The nRF24L01+ transceiver module communicates using serial peripheral interface (SPI) over a 4-pin full duplex protocol allowing for data to be transferred in both directions simultaneously (Last Minute Engineers, n.d.-a). SPI is a synchronous serial communication interface specification using a master-slave architecture with a single master and one or more slaves. The master will synchronize the clock cycle for the output of data bits in which the slave cannot initiate a data transfer unless it notifies the master through an interrupt (Circuit Basics, n.d.). The module's "frequency channel (125 selectable channels), output power (0 dBm, -6 dBm, -12 dBm or -18 dBm), and data rate (250kbps, 1Mbps, or 2Mbps) can be configured through SPI interface" (Last Minute Engineers, n.d.-a).

4. Power Amplifier and Low Noise Amplifier

The Power Amplifier (PA) boosts "the power of the signal being transmitted from the nRF24L01+ chip while the Low-Noise Amplifier (LNA) takes extremely weak and uncertain signal from the antenna and amplifies it to a more useful level" (Last Minute Engineers, n.d.-a). The LNA increases the amplitude of the received signal without increasing the background noise that is associated with the bandwidth which a clearer received RF signal. Viewing Figure 16, the LNA is connected to the receive path while the PA is connected to the transmit path. The two paths are connected by a duplexer before connecting to the antenna. The duplexer separates the transmitter and receiver signals from interfering especially preventing the PA from overloading the lower power of the LNA (Last Minute Engineers, n.d.-a).

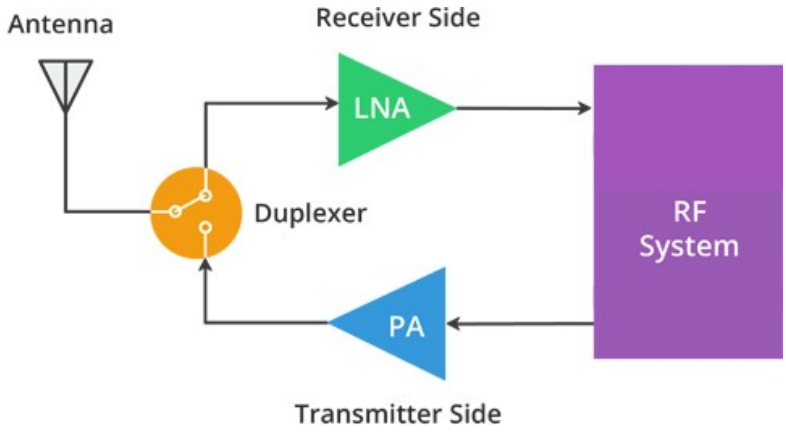

Figure 16. Basic implementation of the power amplifier and low noise amplifier for the transceiver. Source: Last Minute Engineers (n.d.-a).

b. nRF24L01+ Transceiver Operation

As mention in the hardware section, the module "transmits and receives data on a certain frequency called channel" (Last Minute Engineers, n.d.-a). Multiple transceivers need to be on the same channel in order to transmit and receive data between each module. This channel could be any frequency in between 2400 to 2525 MHz in the nRF24L01+ module. There are two features that transceiver module is comprised of which are creating a multiceiver network and Enhanced ShockBurst protocol.

The nRF24L01+ module operates as a multiceiver, which "is an abbreviation for Multiple Transmitters Single Receiver where within each channel there are six parallel data pipes with each pipe having its own data pipe address" (Nordic Semiconductor, 2008, pg. 37). The frequency channel and physical data pipe address for each module can be set by source code in the Arduino IDE. Figure 17 demonstrates the multiceiver network architecture. The NRF Rx in Figure 17 is hub receiver in the network, which collects information from the six different transmitter nodes (NRF Tx) simultaneously because each module is set to its own data pipe (Last Minute Engineers, n.d.-a). The hub receiver can stop acting as the receiver and can be used as a transmitter but can only send information to one module at a time. This multi transmitter and one receiver network is the foundation that the acoustic sensor node network uses to transmit data in order to calculate the triangulation for bomb impact.

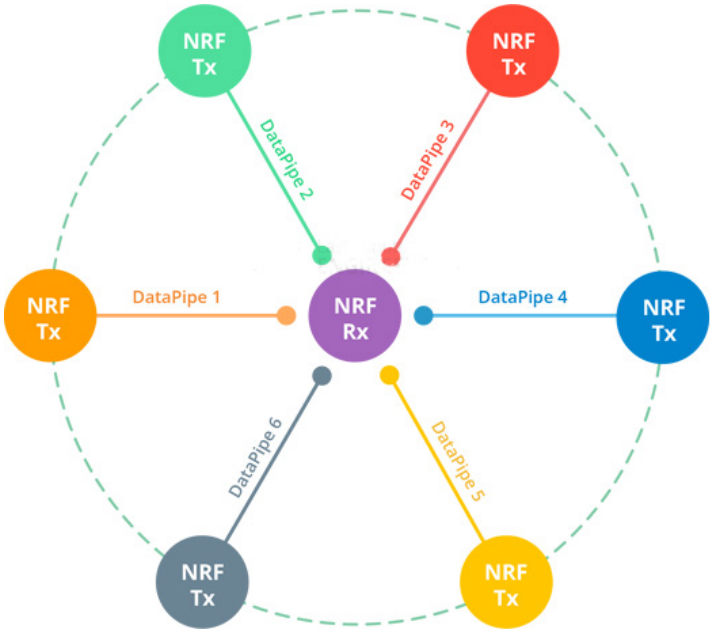

Figure 17. nRF24L01+ multiceiver network diagram. Source: Last Minute Engineers (n.d.-a).

For packet handling, the nRF24L01+ transceiver module uses Enhanced ShockBurst for a packet structure with packet buffering, automatic transaction handling, packet acknowledgments, and automatic retransmissions (Nordic Semiconductor, 2008). The Enhanced ShockBurst packet structure is broken into five fields: “Preamble, Address, Payload and the Cyclic Redundancy Check (CRC) fields and Packet Control (PCF)” (Last Minute Engineers, n.d.-a). Figure 18 is a representation of the packet structure for Enhanced ShockBurst Protocol. The preamble is a sequence of altering bits that ensures the devices on the network have synchronize clocks for transmission and receiving data (Last Minute Engineers, n.d.-a). The address block which can be coded in the Arduino IDE is set to the receiving node to ensure that proper destination node receives the packet. The PCF consists of the payload length, packet ID, and a no acknowledgement flag. The payload length uses a six bit sequence to show the length of the payload of the data. The Enhanced ShockBurst puts a packet ID for each packet during transmission so that the receiving device can determine if the message is new or if it’s a retransmitted message due to a packet loss or interruption (Last Minute Engineers, n.d.-a). The payload field can vary from 0-32 bytes which contains the content of the message being transmitted and received

(Last Minute Engineers, n.d.-a). The protocol allows packet acknowledgment to ensure that packets have been received by the destination node. The last portion of the packet structure is the CRC which is an error detecting code that determines if there is changes to the content of the packet. If the CRC fails then the packet will not be received by the protocol (Nordic Semiconductor, 2008).

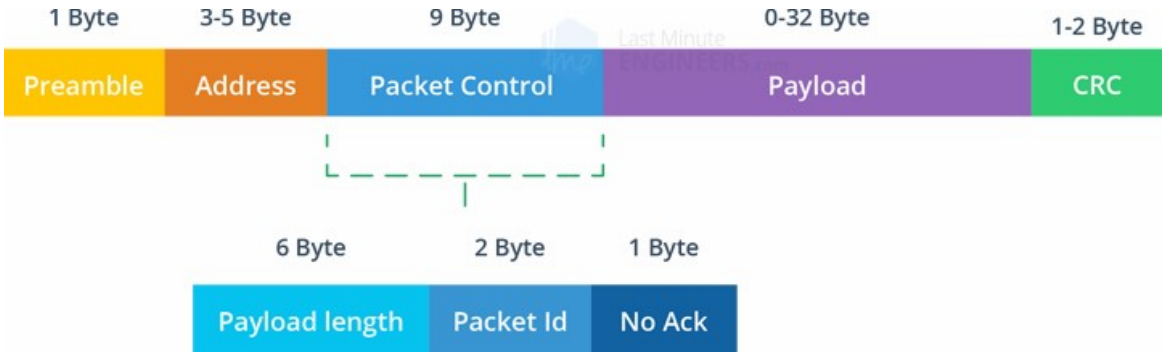

Figure 18. Enhanced shockburst packet structure. Source: Last Minute Engineers (n.d.-a).

The nRF24L01+ has a prebuilt library compatible with Arduino that is opensource to utilize the potential of the radio module for many applications. The sensor network consists of multiple nRF24L01+ transmitters and one nRF24L01+ receiver hub. Each transmitter is wired to an Arduino along with a GPS module and the MEMS DF Acoustic Sensor. The nRF24L01+ transmitter sends data to the hub receiver when a sound source has been detected, which provides the hub receiver with information to calculate the localization of the sound source.

3. Global Positioning System Module

Global Position System (GPS) is attached to each sensor node so that the location of the node can be used in the calculation of the triangulation of the sound source. The GPS modules used for the sensor node system is the NEO-6M GPS module designed by ublox. The NEO-6M module is compact in size (module size 23 mm x 30 mm and antenna size 25 mm x 25 mm) and operates with low power usage but still provides reliable GPS location at effective cost of $16.00-$20.00 (Random Nerd Tutorials, 2017). The unit has a

horizontal positions accuracy of 2.5 m, operates with low power of 2.7 to 3.6 V, and has a receiver type that can track 22 satellites on 50 channels (Last Minute Engineers, n.d.-b). The module has a cold start of 26 seconds or a hot start of 1 second and can do 5 location updates with a Time-To-First-Fix (TTFF) of under a second due to the navigation sensitivity of -161 dBms (u-blox, 2011). The NEO-6M is compatible for Arduino with a prebuilt opensource library.

Figure 19. ublox NEO-6M GPS module. Source: u-blox (2011).

The NEO-6M transmits data through the TX port to the Arduino and receives GPS data through the RX port. Through trilateration, the module receiver calculates the distance from the GPS module to at least three GPS satellites in orbit over 20,000 km through the time it takes for a signal to arrive back to the module (Random Nerd Tutorials, 2017). Once the GPS module receives signals from at least three satellite, it can pinpoint the location of module on Earth. The NEO-6M GPS displays GPS data on the Arduino Serial Monitor using decimal degrees for the latitude and longitude coordinates. As mention before, each sensor node has a NEO-6M GPS module that provides the location of the sensor node to the hub receiver. When a sound source is recorder by the MEMS DF Acoustic Sensor, the direction of the sound along with the sensors GPS coordinates is transmitted to the hub receiver so that it is used for triangulation calculations.

4. Microcontroller

The Arduino microcontroller is at the core of the sensor node device that connects all the components together to execute the operation of the sensor device. The Arduino executes the program code stored on the microcontroller in order to translate information being accumulated into readable material. Each sensor node has one Arduino Uno or Nano to run the code of the device. Figure 20 shows the circuitry of the components of the sensor boxes with the Arduino. The circuitry was based on the design by Professor Peter Crooker in the Physics Department, Naval Postgraduate School (P. Crooker, PowerPoint Slides, October 4, 2018). When the MEMS DF acoustic sensor detects a sound source, the program executes using the voltage produced by the sensor capacitors into an angle of arrival of the sound source. During the operation, the GPS module receives location data from the GPS satellites for the current to coordinates of the sensor node. With the sound source angle of arrival and the GPS coordinates of the sensor node device, the Arduino sends the data using the nRF24L01+ transceiver module to the hub receiver. The hub receiver, an Arduino connected to a CPU, compiles all information received from the sensor node devices that have "heard" a sound source. The hub receiver plots the location of the sensor and the angle of arrival on an interface program. When two direction angles intersect one another, indicating a bomb impact, the GPS coordinates are calculated using a triangulation formula discussed later in this chapter. The information is entered and managed on the mapping interface for visual representation of the current situation.

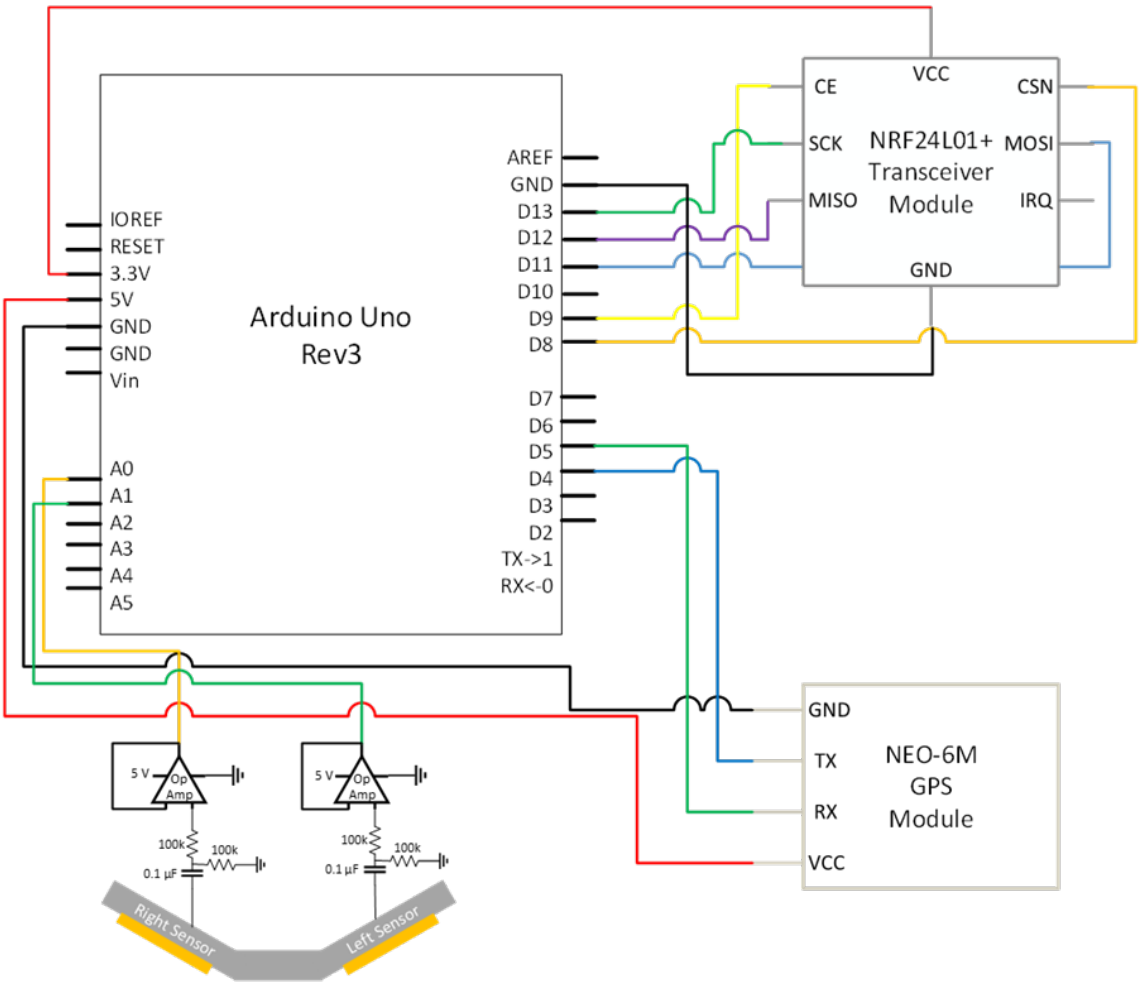

The circuitry overview includes the connections with the DF MEMS sensors, NEO-6M GPS module, and the nRF24L01+ transceiver module.

Figure 20. Circuit overview for the sensor node.

5. Sensor Node Cost Estimation

The components for the sensor node and hub receiver are made up of low cost materials but maintain a high quality of performance to meet the standards for the project. Table 1 and Table 2 show the estimated price for an individual sensor node and for the hub receiver, which is currently priced to be $151.00 and $27.00, respectively. The estimations do not take into the account that more batteries will be needed for the sensor node since a 9V battery is used and the battery will eventually drain. The hub receiver is connected to an electrical source such as a laptop so that the MATLAB displays the location of the impact on a mapping interface. Figure 21 shows the design of the sensor box comprised

with the MEMS DF Sensor, the nRF24L01+ transceiver, and the NEO-6M GPS module. The sensor box structure used in this research is based on the design by Professor Peter Crooker in MEMS Sensor Workshop at the Naval Postgraduate School (PowerPoint Slides, October 4, 2018). The box was designed using AutoCAD Fusion 360 and fabricated with the Ultimaker 3 3D Printer using polylactic acid (PLA) filament as the material used for the structure of the box.

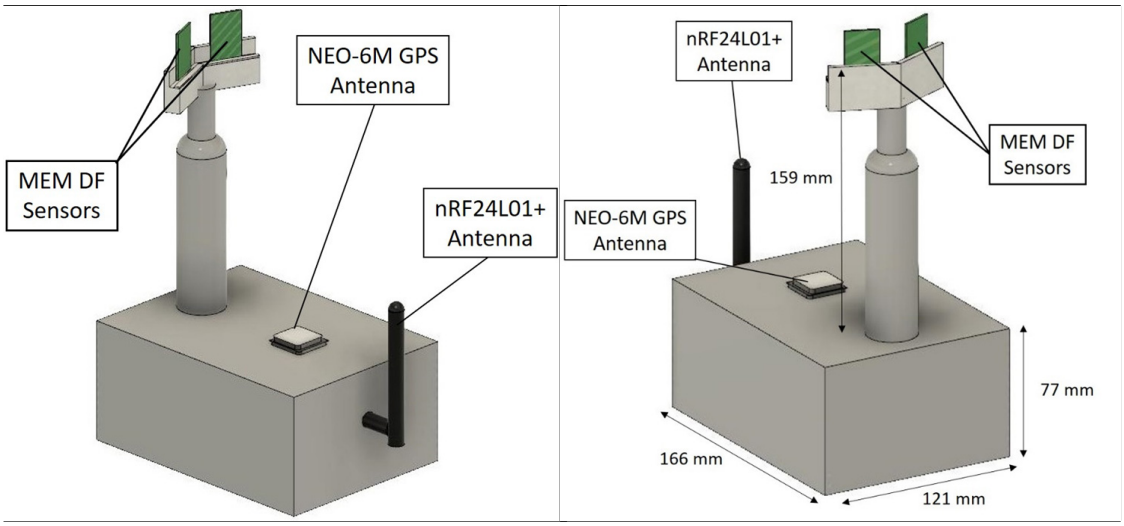

Figure 21. Sensor node design

Table 3. Sensor node estimated price

Main Components	Price (US)
MEMS DF Acoustic Sensor (estimation if mass production is available)	$ 50.00
nRF24L01+ Transceiver Module	$ 5.00
NEO-6M GPS Module	$ 20.00
Arduino Uno Rev3	$ 22.00
Basic Components	
Housing Box	$ 10.00
Electrical (resistors, wires, capacitors, breadboards)	$ 20.00
Sensor Mount	$ 15.00
Battery	$ 9.00
Total Estimate Price per Sensor Node	**$ 151.00**

Table 4. Hub node estimated price

Main Components	Price (US)
nRF24L01+ Transceiver Module	$ 5.00
Arduino Uno Rev3	$ 22.00
Total Estimate Price per Sensor Node	**$ 27.00**

C. TRIANGULATION ALGORITHM FOR LOCALIZING SOUND SOURCE

Determining the location of the impact of an ordinance, a triangulation algorithm is used which incorporates at least two sensor nodes with fixed locations. When a bomb impacts, the MEMS DF acoustic sensors calculate a bearing to the impact location. The

bearings from the sensor nodes eventually intersect in which the intersection is the possible location of the bomb impact. Trigonometry is used because of the fixed coordinates of the sensor which will be referenced in latitude and longitude and the azimuths to the sound source. Figure 22 shows the formation of a triangle through the two known points and the intersection of the bearings from each node, providing the necessary variables to the compute the latitude and longitude of the impact.

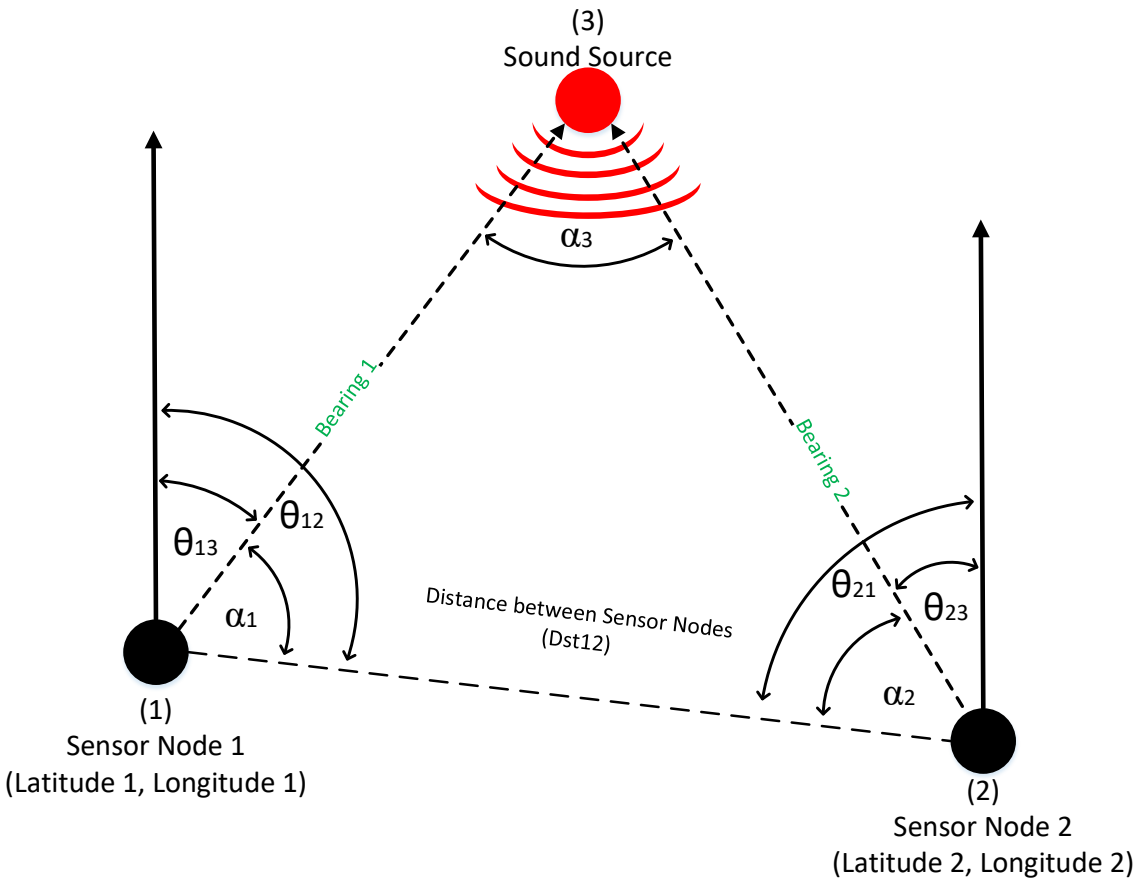

Figure 22. Triangulation determined by intersection of two bearings from two known locations

Since the latitude and longitude of the sensors is known, the first part of the algorithm is to calculate the distance between the two sensors using the haversine formula. When using trigonometry functions with programming languages such as python and C, the arguments in the trigonometry functions use radians as the variables. Because of this,

latitude, longitude, and the bearings will need to be converted from degrees to radians (Veness, 2019). The haversine formula (Equation (3)) is used for spherical Earth navigation in which it calculates the distances between two pairs of coordinates on a sphere (Mahmoud & Akkari, 2016).

$$dst_{12} = 2r\ arcsin\sqrt{sin^2\left(\frac{\varphi_2 - \varphi_1}{2}\right) + \cos(\varphi_1)\cos(\varphi_2)\,sin^2\left(\frac{\lambda_2 - \lambda_1}{2}\right)} \quad (3)$$

In Equation (3), r is the radius of the sphere which is the earth in this reference while the latitude and longitude of sensor 1 is φ_1 and λ_1, respectively, and latitude and longitude of sensor 2 is φ_2 and λ_2, respectively (Mahmoud & Akkari, 2016). The next step in the algorithm is to calculate the initial and final bearing between points 1 and 2, which are the sensors in Figure 22. These bearings will eventually assist in computing the angles α_1, α_2, and α_3 which are the interior angles that form a spherical triangle in Figure 22. To calculate the initial bearings between the two points, use Equation (4) and Equation (5) where θ_a is the initial bearing from point 1 to point 2 and θ_b is the initial bearing from point 2 to point 1 (Veness, 2019).

$$\theta_a = acos((\ sin(\varphi_2) - sin(\varphi_1) \cdot cos(d)\ ) / (\ sin(d) \cdot \cos(\varphi 1)) \quad (4)$$

$$\theta_b = acos((\ sin(\varphi_1) - sin(\varphi_2) \cdot cos(d)\ ) / (\ sin(d) \cdot \cos(\varphi_2)) \quad (5)$$

To get the final bearing between point 1 and point 2, the azimuth and reverse azimuth between the two points are calculated using Equation (6) where θ_{12} is the bearing from point 1 to point 2 and θ_{21} is the bearing from point 2 to point 1. By taking the sine of the longitude difference determines which bearing needs to be the reverse azimuth (Veness, 2019).

$$
\begin{aligned}
&if\ \sin(\lambda_2 - \lambda_1) > 0 \\
&\quad \theta_{12} = \theta_a \\
&\quad \theta_{21} = 2\pi - \theta_b \\
&else \\
&\quad \theta_{12} = 2\pi - \theta_a \\
&\quad \theta_{21} = \theta_b
\end{aligned} \tag{6}
$$

After calculating θ_{12} and θ_{21}, these variables are used to calculate the interior angles α_1 and α_2 in Equations (7) and (8) by taking the azimuth difference of θ_{13} and θ_{12} and azimuth difference of θ_{21} and θ_{23} (Federal Aviation Administration [FAA], 2016).

$$\alpha_1 = \theta_{13} - \theta_{12} \tag{7}$$

$$\alpha_2 = \theta_{21} - \theta_{23} \tag{8}$$

Because θ_{13}, θ_{12}, θ_{21}, and θ_{23} are bearings, there values go from $-\pi$ to $+\pi$ or -180° to +180°. To get the proper angle calculations for α_1 and α_2, the bearing values need to be converted to 0 to 2π or 0° to 360° using a modulo operation which is done in Equations (9) and (10) as well as taking the absolute values of operation (Veness, 2019). The α_1 and α_2 calculated in Equations (7) and (8) are then used in Equations (9) and (10). The values of α_1 and α_2 are used to calculate the final interior angle of Figure 22, which is α_3 Equation (11) (Veness, 2019). To calculate the new latitude and longitude of the sound source, a distance from either point 1 or point 2 to point 3 must be calculated using Equation (12), which solves the distance from point 1 to point 3.

$$\alpha_1 = |(\alpha_1 + 2\pi \; or \; 360°) \; modulo(2\pi \; or \; 360°)| \quad (9)$$

$$\alpha_2 = |(\alpha_2 + 2\pi \; or \; 360°) \; modulo(2\pi \; or \; 360°)| \quad (10)$$

$$\alpha_3 = \text{acos}\big(-cos(\alpha_1) * cos(\alpha_2) + sin(\alpha_1) * sin(\alpha_2) * cos(dst_{12})\big) \quad (11)$$

$$dst_{13} = (atan2(\sin(dst_{12}) * \sin(\alpha_1) * \sin(\alpha_2), \cos(\alpha_2) + \cos(\alpha_1) * \cos(\alpha_3)) \quad (12)$$

With the distance between point 1 and 3 calculated, the latitude (φ_1) and longitude (λ_3) of the sound source is determined with Equations (13), (14), and (15) (Veness, 2019). When taking the arc tangent, its output values have a range of -π to +π or -180° to +180°. Because of this, the longitude difference ($\Delta\lambda_{13}$) calculated in Equation (14) is normalized with the modulo operation in Equation (15) to get the final longitude (λ_3) of the sound source.

$$\varphi_3 = asi\,n(sin(\varphi_1) * cos(dst_{13}) + cos(\varphi_1) * sin(dst_{13}) * cos(\theta_{13})) \quad (13)$$

$$\Delta\lambda_{13} = atan2(\sin(\theta_{13}) * \sin(dst_{13}) * \cos(\varphi_1), \cos(dst_{13}) - \sin(\varphi_1) * \sin(\varphi_3)) \quad (14)$$

$$\lambda_3 = \lambda_1 + \lambda_{13} \quad (15)$$

1. Python PyGeodesy Triangulation

The triangulation algorithm based on two know points with two bearings just reviewed in the last section has already been designed and implemented in a Python application called PyGeodesy which is a collection of tools and functions for ellipsoidal and spherical models including Earth spherical models (Brouwers, 2016). The PyGeodesy application provides calculations to determine distances, bearings, ellipsoidal and spherical points of reference, coordinate conversions and much more as well as a function to determine the intersection of two bearings from two known points (Brouwers, 2016).

The equations and calculations used for this project in PyGeodesy are based on "A Non-singular Horizontal Position Representation" by Kenneth Gade (Brouwers, 2016).

Position calculations such as latitude and longitude, UTM, and local Cartesian can lead to errors when determining positions due to the shape of the earth. Latitude and longitude positions have errors when calculating near the pole singularities and as well using the ellipsoidal Earth model (Gade, 2010). UTM and local Cartesian calculations are complex and prone to errors in accuracy when computing positions over long distances with the flat Earth models (Gade, 2010). To overcome the errors with coordinate systems just mention, PyGeodesy uses normal vector (n-vector) which represents horizontal position on the earth's surface by a vertical-perpendicular frame to calculate position (Gade, 2010). Figure 23 represents the horizontal position on the Earth model using the n-vector. The n-vector calculations are simplified using dot and cross product algebra, which the results reference a position on Earth and can be easily converted to latitude and longitude coordinates (Gade, 2010). The software of the sensor network incorporates the intersection function of Pygeodesy to triangulate the sound source.

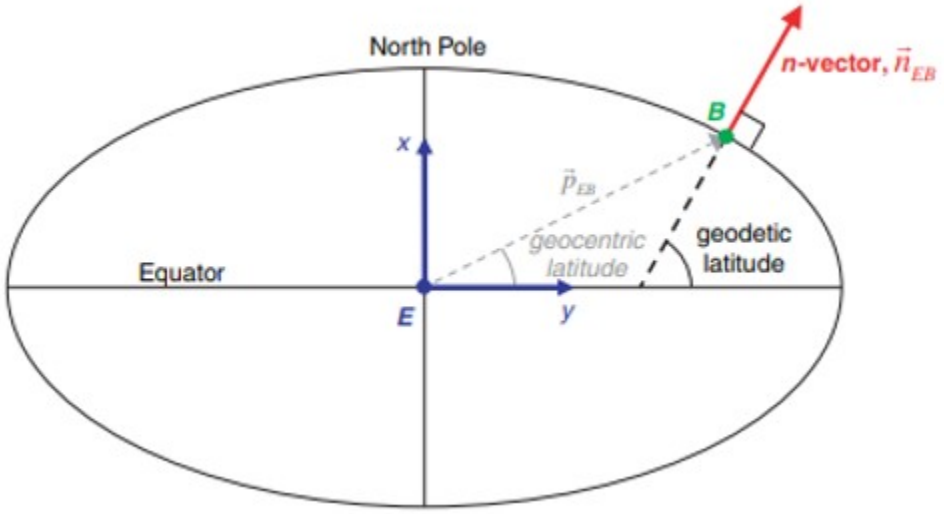

Figure 23. Horizontal position is represented by the vertical vector from the surface tangent plane on the Earth model. Source: Gade (2010).

2. MATLAB Mapping Toolbox

The Mapping Toolbox of MATLAB creates map displays through manipulation and customization of geographic data encompassing vector and raster Geographic

Information Systems (GIS) and geospatial data. The toolbox also has functions and geodetic algorithms to analyze geospatial data in order to calculate distances, directions, areas, special curves, and intersections on a spheroidal or planar surface. MATLAB's map display and functions are used to show the location of a sound source on a map interface with reference to the intersection of bearings from the known positions of the sensor nodes. The specific function used in the mapping display is the intersection of rhumb line tracks, which uses known location points and rhumb line azimuths for calculations. Rhumb lines are lines on the earth's surface that crosses each meridian at the same angle, which covers more distance than following geodesic line or great circle but has a constant bearing unlike great. Each sensor node has a known reference point of latitude and longitude with an azimuth towards the sound source. The azimuth is measured clockwise in relation to True North and is the angle a line makes with a meridian. The function takes the intersection of the rhumb lines and produces a latitude and longitude for the intersection point representing the sound source location. This intersection is displayed on an aerial imagery map with the latitude and longitude coordinates for visualization purposes.

D. SYSTEM PROCESS AND INFORMATION FLOW

This section discusses the data flow process from the sensor nodes relaying information to the hub receiver. With the received data, MATLAB executes the triangulation function and created a visual map of the sound source location. As previously mentioned, each sensor node is comprised of two MEMS DF Sensors, one NEO-6M GPS Module, one nRF24L01+ Transceiver, and one Arduino Uno or Nano while the hub receiver is comprised of an Arduino Uno and a nRF24L01+ Transceiver connected to a laptop. On the laptop, the MATLAB mapping toolbox and Python Pygeodesy programs execute function calculations and creates the map displays. Figures 24, 26, 27, and 28 are snapshots from the MATLAB mapping toolbox as the program is run at the Camp Roberts McMillan Airfield through the steps of the code using the map display functions and the triangulation calculations.

When the network system is initiated, each sensor node transmits the latitude and longitude coordinates in decimal degrees using the nRF24L01+ transceiver to the hub

receiver. Each sensor node has its own unique ID number allowing the mapping program to identify the proper sensor nodes. The location of the sensor displays on the mapping interface for visual purposes and the GPS location of a sensor is stored as a variable to be used for the location calculations when a sound source is processed. Figure 24 demonstrates the MATLAB mapping toolbox creating a geographic aerial imagery map and plotting the location of the sensors.

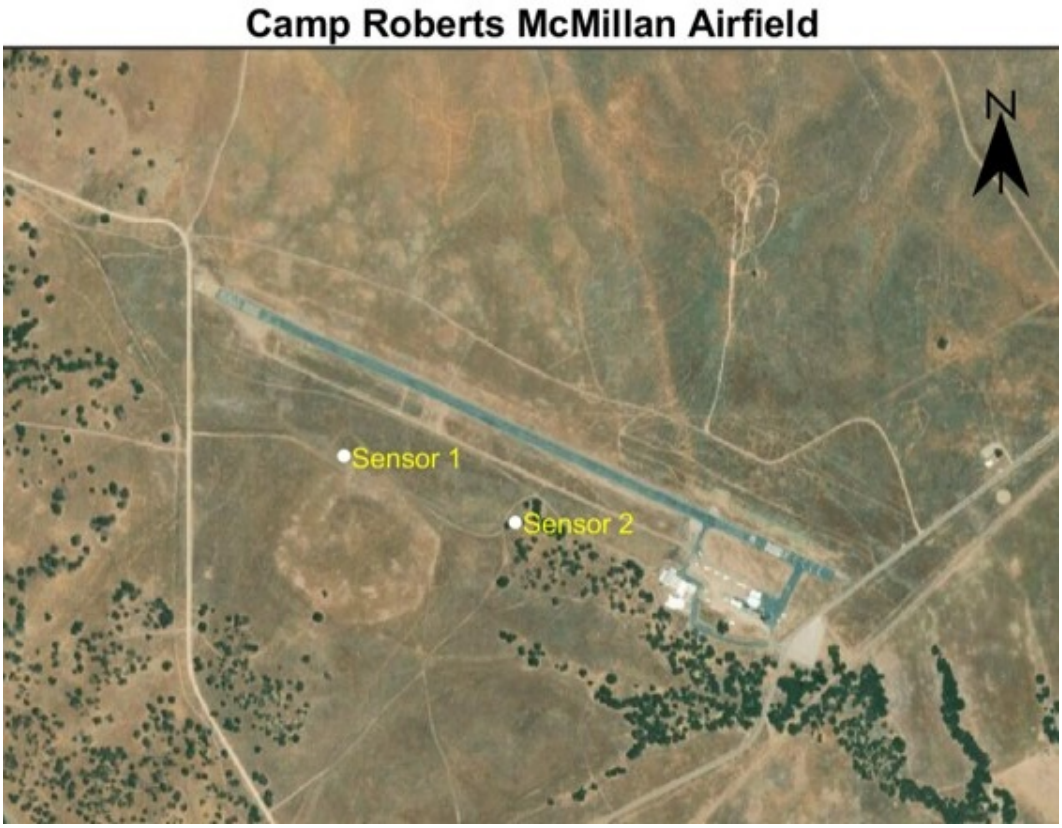

Figure 24. MATLAB mapping interface displaying the locations of the sensors

When the income sound wave reaches a pre-established threshold, the MEMS DF acoustic sensor output voltages are read by the Arduino microprocessor that executes the direction of arrival algorithm and then transmits the bearing angle from the sound sensor node to the hub receiver. Stored as a variable in the mapping program, the bearing angle is then used in the triangulation algorithm. The sound sensor nodes transmit along with the

bearing the ID number, latitude, and longitude of the sensor node represented in Figure 25. The mapping program draws a bearing angle on the map interface from each sensor node until there is an intersection between the two lines. Figure 26 shows the bearing angles indicated by the green line from each sensor node and an intersection point of the two angles.

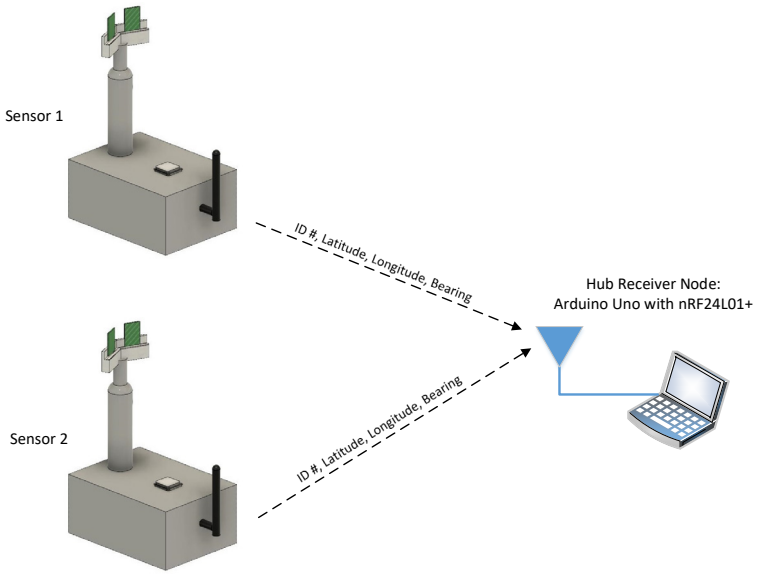

Figure 25. Ground sensor node transmission of ID number, latitude, longitude, and bearing to the hub receiver node

The bearing angle from each sensor is drawn on the map display until the lines intersect to indicate the location area of the sound source.

Figure 26. MATLAB mapping interface displaying bearing angle lines

With the two bearings from the two known points transmitted and received, the localization of the sound source is computed. Using the intersection function of the MATLAB program and PyGeodesy script, the intersection point, indicating the general area of the sound source, is calculated. The result is the latitude and longitude of the intersection and places a marker on the map display for visual reference. Figure 27 show the marker placement for the intersection point of the bearing lines indicating the area of the bomb impact. MATLAB and PyGeodesy provides the latitude and longitude via text and places the coordinates on the map display shown in Figure 27.

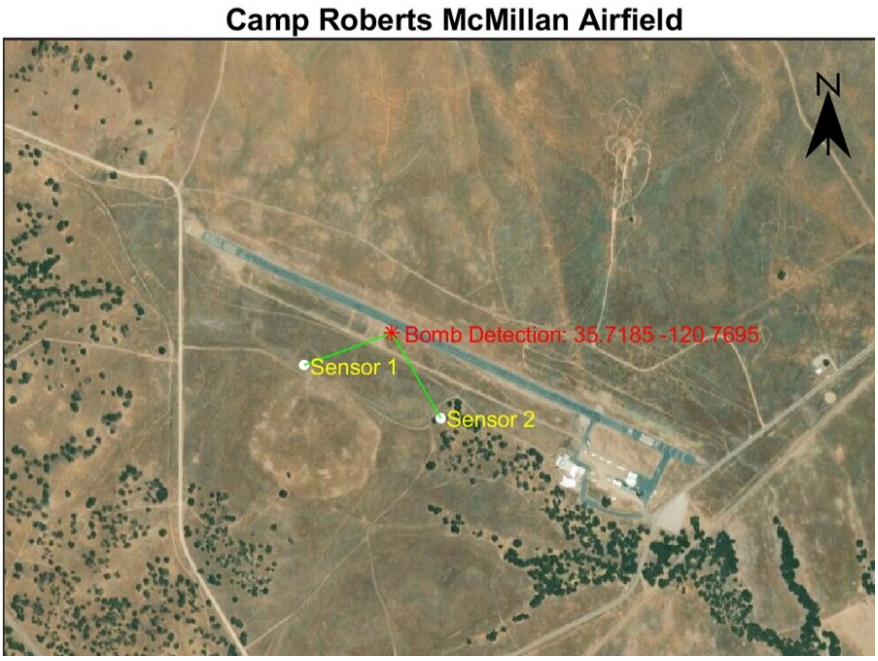

Figure 27. MATLAB mapping interface using intersection function to determining latitude and longitude of intersection

The equipment and software tools used for the experiment produce results that are easily identifiable and instantaneous which help increase the speed and accuracy of the ADA process.

E. SUMMARY

This chapter discussed the components of the sensor network specifically the equipment used for each sensor node and the programs and software for mapping and mathematical calculations. The cost of the project materials is low with each sensor node to be estimated to cost $151.00 (if the MEMS sensor is mass produced), while the equipment needed for the hub receiver is estimated to be $27.00. The components and design allow the system to be easily deployable, require low power consumption, and be easily manageable for the purpose of the experiment. The instantaneous and autonomous capability of the system to detect and triangulate bomb impacts would increase the ADA process speed and accuracy which in turn helps the recovery process of the airfield. Chapter IV provides the experimentation and testing of the system which was conducted at the

Naval Postgraduate School in Monterey, California. The chapter elaborates how the system functions and reacts in a real time environment to detect and triangulate a sound source.

IV. IMPLEMENTATION AND TESTING

This chapter presents the implementation, experimentation and testing of the ground acoustic sensor network system. The tests were performed in an anechoic chamber and outdoors in the field. The findings during the experimentation process is discussed to include accuracy, limitations, and other noteworthy observations. The chapter concludes with an overall assessment and performance of the system.

A. PURPOSE OF EXPERIMENTATION

The purpose of the experimentation is to test the accuracy and speed of the ground acoustic sensor network system that includes testing the accuracy of the MEMS DF acoustic sensors, the consistency of transmitting data from the ground sensor nodes to the hub receiver, and the accuracy of the triangulation and mapping in MATLAB.

1. Measurements and Analysis

To ensure the proper performance measurement of the system, different measurements are taken to analyze the accuracy and precision of the components of the network sensor system. The components that are key to the accuracy of the triangulation and localizing the sound source are the DF MEMS acoustic sensor and the GPS module for each individual sensor. As mentioned in the system process flow in Chapter III, Paragraph D, the triangulation algorithm is based on the location of two known points with bearing from each point to the sound source. The intersection of the two bearings is the approximate location of the sound source.

a. GPS

For the GPS module to get a proper signal from the satellites that are being used for trilateration, the modules need to have a clear view of the sky with no large structures nearby. Precise location of an object depends on the number decimal places for the latitude and longitude coordinates. Table 5 provides the approximate distance accuracy for the number of decimal places for the degrees in latitude and longitude. A coordinate with no decimal places gives an approximate location precision of 111 km, which would equate to

having an overview location of a small state in the U.S. To get accurate results for our calculations, at least five decimals are needed which gives approximate accuracy distance of 1.11 meters. The fewer decimals provided in the triangulation algorithm, the less accurate the results to the sound source location are.

Table 5. Decimal degree precision and conversion to distance. Source: U.S. Naval Academy [USNA] (2017).

Decimal Places	Degrees	Approximate Distance
0	1	111 km
1	0.1	11.1 km
2	0.01	1.11 km
3	0.001	111 m
4	0.0001	11.1 m
5	0.00001	1.11 m
6	0.000001	0.11 m
7	0.0000001	0.011 m

b. MEMS DF Acoustic Sensor

The MEMS DF Acoustic Sensor can be much more sensitive than high end conventional microphones (Alves & Karunasiri, 2018), allowing the detection of sound sources from very far distances. The resonant characteristic of the sensor provides intrinsic filtering of acoustic sources outside the spectral range of interest. Though with these capabilities, there is still a possibility for the sensor to detect a false positive sound wave or capture the reflection of a sound wave which results in the inaccurate calculation in the bearing angle. In the performance tests, bearings that are calculated by the sensor need to be compared with the actual angle to verify the accuracy before further calculations are executed. Measured bearing and actual bearing are collected throughout the experiment to determine the error percentage which can be applied to the accuracy of the triangulation algorithm.

c. Triangulation

The performance of the triangulation, which is an important goal of the experiment depends on many factors. These factors are the accurate positioning of the sensor nodes with the GPS module and the bearing calculation of the MEMS DF acoustic sensors. To get a good qualitative understanding of the system's performance, many test trials with different parameters were conducted. Accuracy and precision associate with one another can understood by analyzing the example shown in Figure 29 (Carlson, 2002).

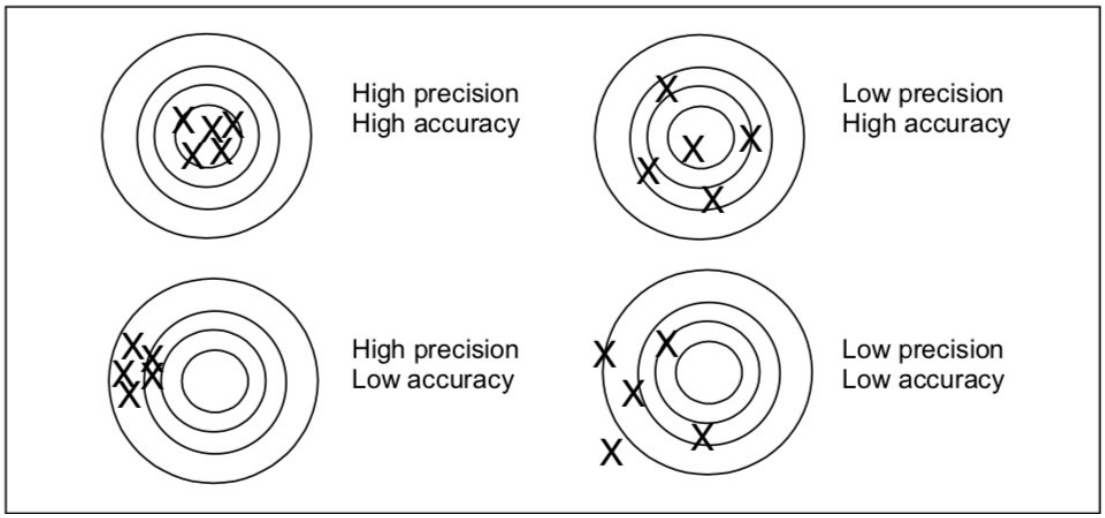

Figure 28. Precision and accuracy with regard to the ground sensor network system. Source: Carlson (2002).

In the figure, the center of the target (bullseye) represent the actual location of the sound source. The 'X' marks represent the locations calculated network system. High precision is obtained when the locations determined by several measurements are very close to each other. Low precision is obtained when the locations are spread (McNeely, 2018). High accuracy is obtained the measured location average is closer to the center of the target where the actual source is. Inaccurate measurements are obtained when the average of the locations is away from the bullseye (McNeely, 2018). The data produced from multiple test trials using different parameters allows us to determine the performance of the system in terms of accuracy and precision. The test results will be used to feedback

the design cycle to improve not only the sensor but also the communication system and localization algorithms.

B. EXPERIMENTATION

Experimentation was conducted using two different setups to include a controlled and uncontrolled environment. The controlled environment tests were performed in an anechoic chamber to eliminate reflection, background noise and simulate targets at a greater distance. The outdoors tests were performed at the NPS baseball field with no environment control to emulate conditions closer to the ones found in the operational environment.

1. Anechoic Chamber Calibration Testing

The anechoic chamber absorbs the sound waves in a wide spectral range, eliminating reflection. In this case, the collected data is only influenced by direct sound and not from reflective sound. The sound used for the excitation was a recording of a bomb explosion, which was found to have a broad band acoustic spectrum that includes the 1.6 kHz resonance frequency of the MEMS DF acoustic sensors. The sensor node was connected to rotator mount approximately five meters away from the speaker. Figure 29 shows a schematic of the anechoic chamber setup and Figure 30 shows actual images of the experimentation. The rotator allows for the rotation of the sensor while the speaker could stay stationary. The rotation was used to verify different angles of arrival when the sound sensor detects the sound wave from the speaker.

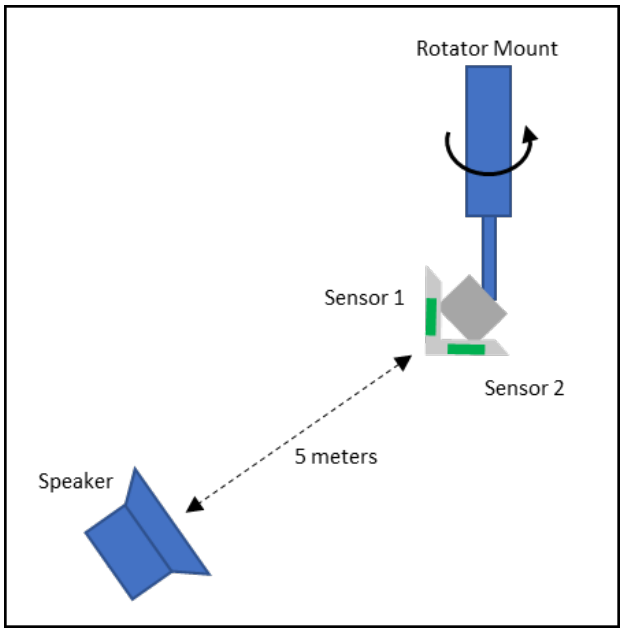

Figure 29. Schematic of the NPS anechoic chamber room setup for calibration testing

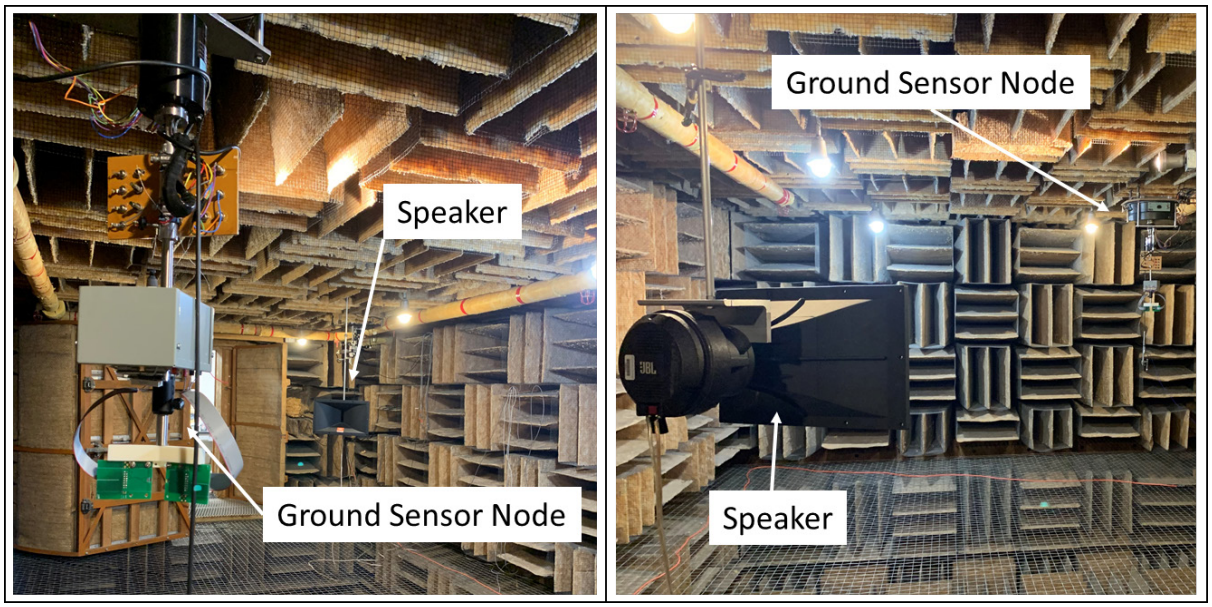

Figure 30. Images of the NPS anechoic room setup

We rotated the sensor +/- 60 degrees in reference to the speaker comparing the measured results to the actual angle to verify the accuracy of the ground sensor node. As mentioned before in Chapter III, Paragraph B, Section 1.c, the capacitors in each MEMS DF acoustic sensors create a voltage from the mechanical displacement of the wings, which exhibits a cosine dependence with the angle of arrival. The node's Arduino reads the voltages from the left and right sensors and performs the calculation of the non-ambiguous bearing.

We have tested two sensor nodes and collected data for angles between +/- 60 degrees and the measurements were compared with actual angles. The experiment was done at increments of +/- 10 degrees with seven trials for each increment to calculate an appropriate average for the measured angle. Table 6 and Table 7 show the results of the experiment. Table 6 also includes the average deviation between the actual and measured angle. Figures 31 and 32 are graphs comparing the measured and actual angles from the experiments with both sensors.

As shown in Table 6, the average error is no higher than 3 degrees, except for angles between 0 and 20 degrees where the error was between 3 and 5 degrees. It can also be observed that the error is systematic and most likely can be corrected by calibration. Figure 31 shows the average measurements at each angle increment compared with the linear line representing the actual angle.

Table 6. Data results comparing the measured angle and actual angle for sensor node 1

Actual Angle	Sensor 1 Measured Angle (°)								
(°)	Trial 1	Trial 2	Trial 3	Trial 4	Trial 5	Trial 6	Trial 7	Avg Measured Angle	Avg Deviation
-60	-58	-58	-60	-59	-58	-59	-59	-58.714	1.286
-50	-51	-51	-51	-51	-51	-50	-49	-50.571	0.571
-40	-40	-39	-39	-40	-41	-41	-39	-39.857	0.143
-30	-30	-30	-30	-31	-31	-31	-31	-30.571	0.571
-20	-21	-21	-21	-21	-22	-21	-21	-21.143	1.143
-10	-12	-12	-13	-12	-12	-13	-12	-12.286	2.286
0	-3	-3	-3	-3	-4	-3	-3	-3.143	3.143
10	6	6	6	5	5	5	5	5.429	4.571
20	15	15	15	15	16	15	16	15.286	4.714
30	27	27	27	27	28	27	27	27.143	2.857
40	39	39	38	38	39	38	38	38.429	1.571
50	49	49	52	50	50	49	50	49.857	0.143
60	60	60	60	59	60	60	59	59.714	0.286

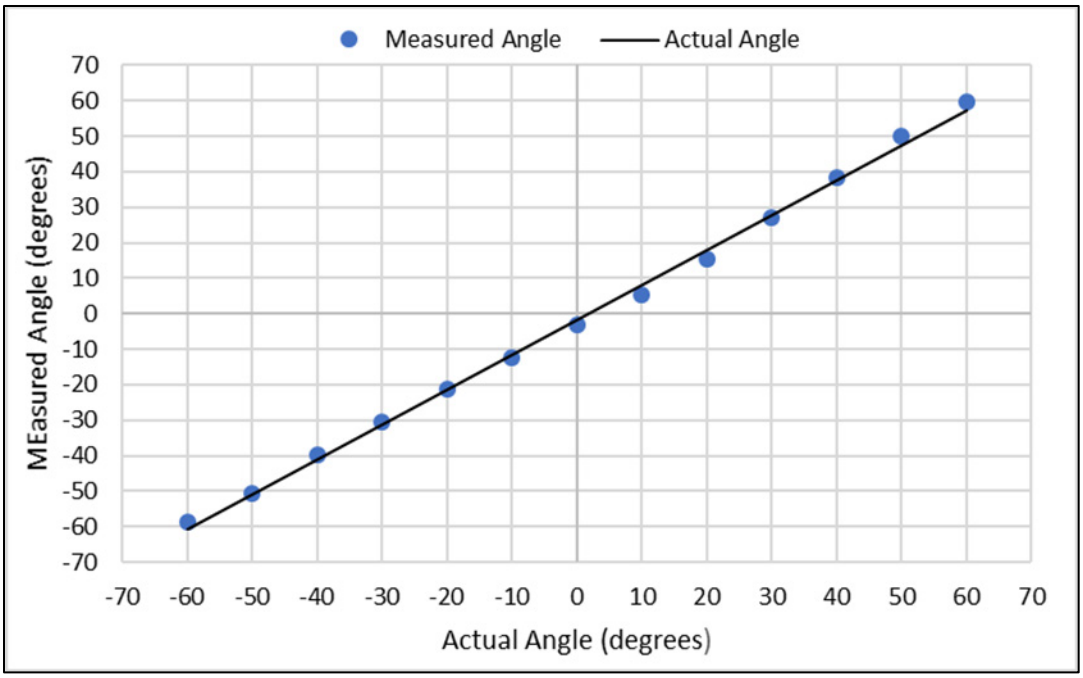

Figure 31. Graph comparing the actual angle and the measured angle for sensor node 1

As shown in Table 7 the maximum error for the second sensor node was 3.00 degrees, measured at -60 degrees. For higher angles, one possible explanation for the error is the reflections off the electrical wires and metallic mounts of the sensor assembly. Figure 32 shows the average measurements at each angle increment compared with the linear line representing the actual angle. Overall, both nodes were found to be adequate for the field test, exhibiting better performance than commercially available acoustic direction finders. Raytheon BBN Technologies created the Boomerang System which uses multiple microphones to detect gunshots within plus or minus 15 degrees (Wilmott, 2015). The MEMS DF sensor demonstrates that is can provide a more accurate reading with an average error no higher than 3 degrees.

Table 7. Data results comparing the measured angle and actual angle for sensor node 2

Actual Angle	Sensor 2 Measured Angle (°)								
(°)	Trial 1	Trial 2	Trial 3	Trial 4	Trial 5	Trial 6	Trial 7	Avg Measured Angle	Avg Deviation
-60	-57	-57	-57	-57	-57	-57	-57	-57.000	3.000
-50	-49	-48	-49	-49	-48	-49	-49	-48.714	1.286
-40	-39	-39	-39	-39	-39	-39	-39	-39.000	1.000
-30	-29	-28	-29	-29	-29	-28	-29	-28.714	1.286
-20	-18	-19	-19	-19	-19	-19	-19	-18.857	1.143
-10	-7	-7	-7	-8	-8	-8	-8	-7.571	2.429
0	2	2	2	1	1	1	2	1.571	1.571
10	10	10	10	10	11	10	10	10.143	0.143
20	20	19	20	20	19	20	20	19.714	0.286
30	30	30	30	30	30	30	30	30.000	0.000
40	40	40	40	40	41	41	40	40.286	0.286
50	51	51	52	52	51	51	50	51.143	1.143
60	60	60	60	60	60	60	60	60.000	0.000

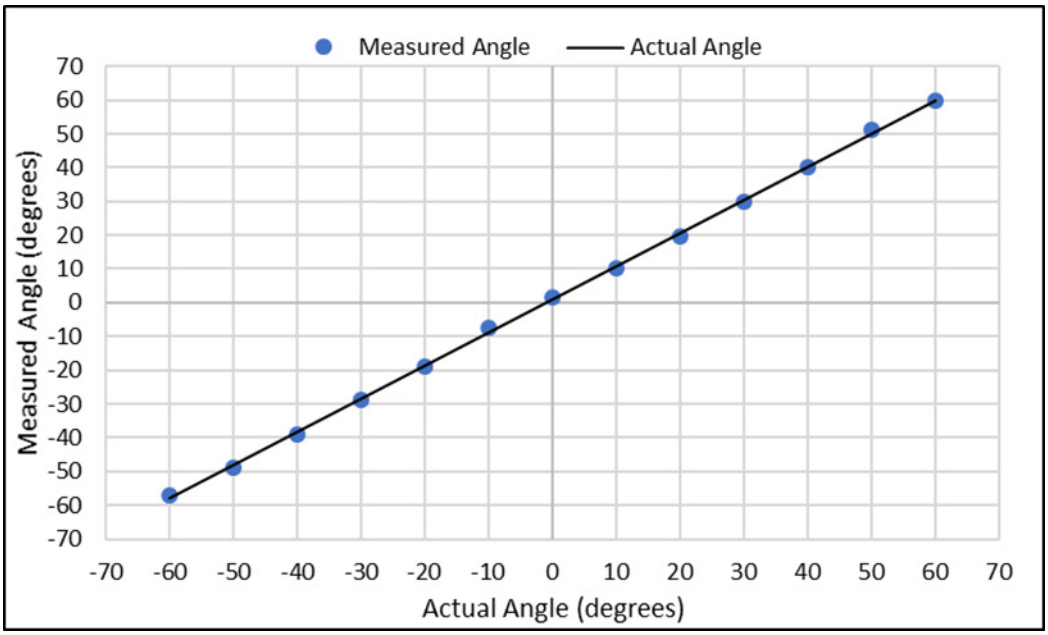

Figure 32. Graph comparing the actual angle and the measured angle for sensor node 2

2. Anechoic Chamber Triangulation Experiment

In the anechoic chamber, we also conducted triangulation experiments using two nodes for detection and the speaker representing the sound of an explosion. A grid system was measured and mapped out to represent locations in the anechoic chamber. During the experiments, sensor node 1 was stationary at the reference point (0,0) and the speaker was stationary at the reference point (72,160). Sensor node 2 was moved to three different points during the tests. Four separate trials were conducted for each location to determine the precisions and accuracy of the triangulation. Figure 33 is a schematic of the setup for the triangulation test in the anechoic chamber while Figures 34 and 35 are images of the anechoic chamber setup.

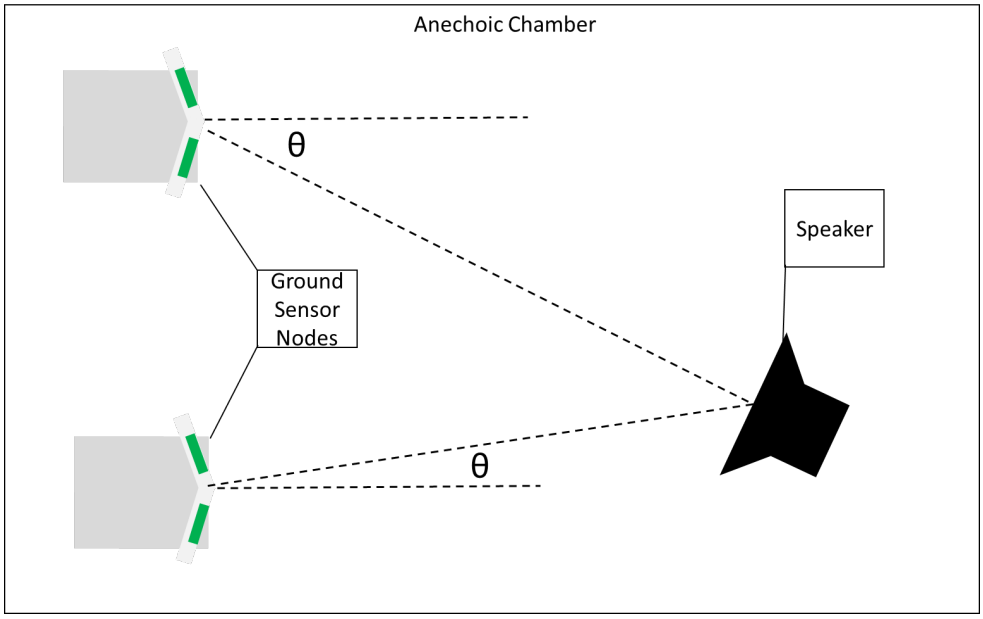

Figure 33. Schematic of the triangulation experiment in the anechoic chamber

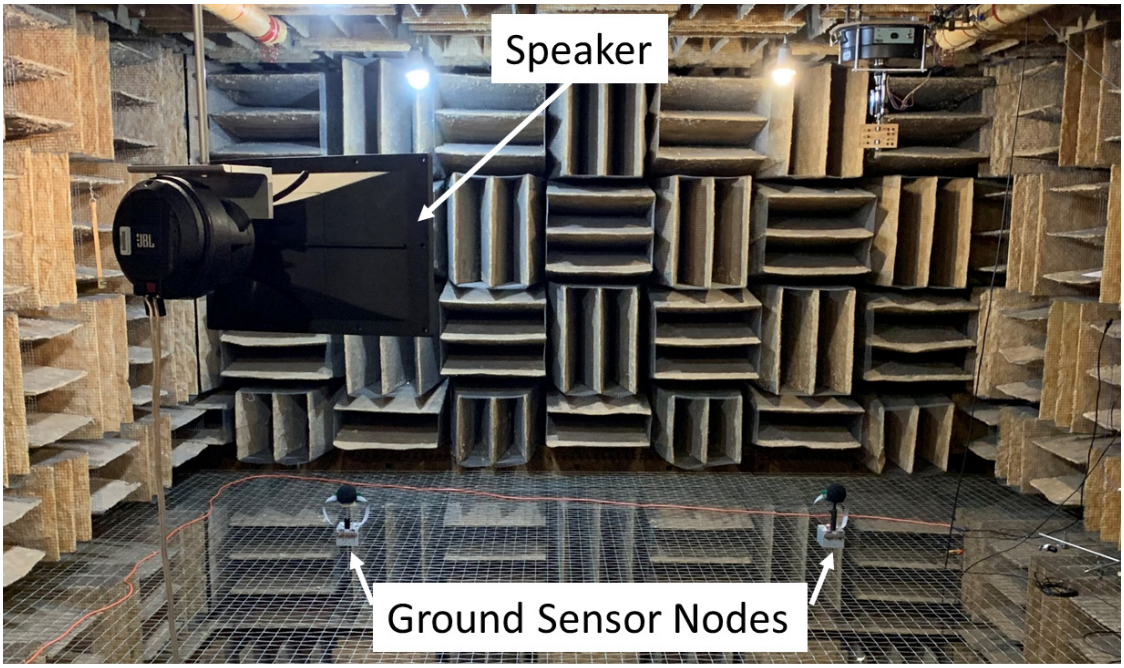

Figure 34. Image of the triangulation experiment in the anechoic chamber

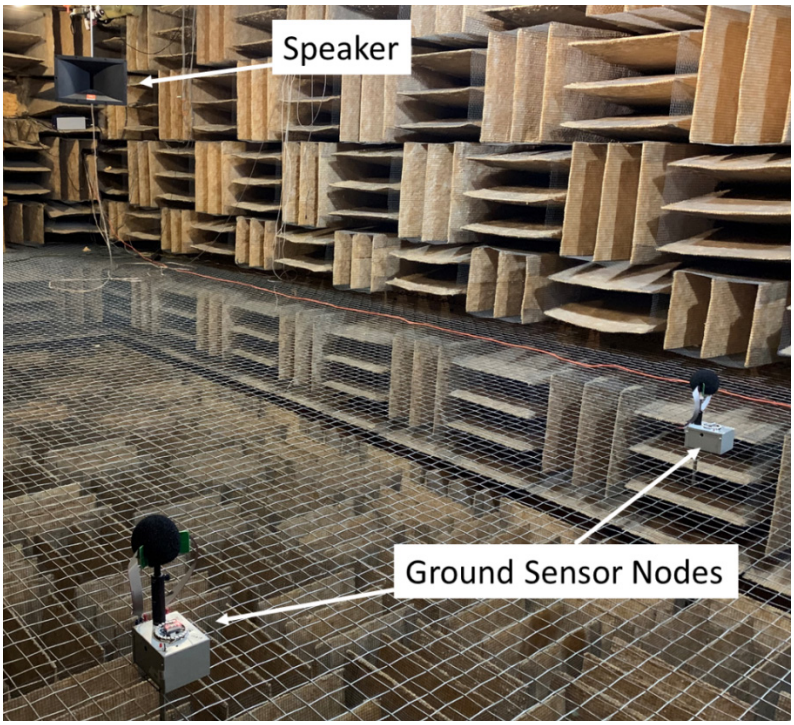

Figure 35. Image of the triangulation experiment in the anechoic chamber

a. Anechoic Chamber Triangulation Test 1

For the first test, sensor node 1 and the sound source are located at their stationary locations while sensor node 2 is located at grid point (84,0). These locations were inputted into MATLAB along with the bearings that are determined during the tests. With the data, MATLAB runs the triangulation calculation to determine the location of the sound source. Test 1 had four different trials. Figure 36 shows the result of the test 1, trial 1 (red circular marker) including the location of the sensor nodes referenced to the grid and as well the actual location of the sound source represented by a blue circular marker.

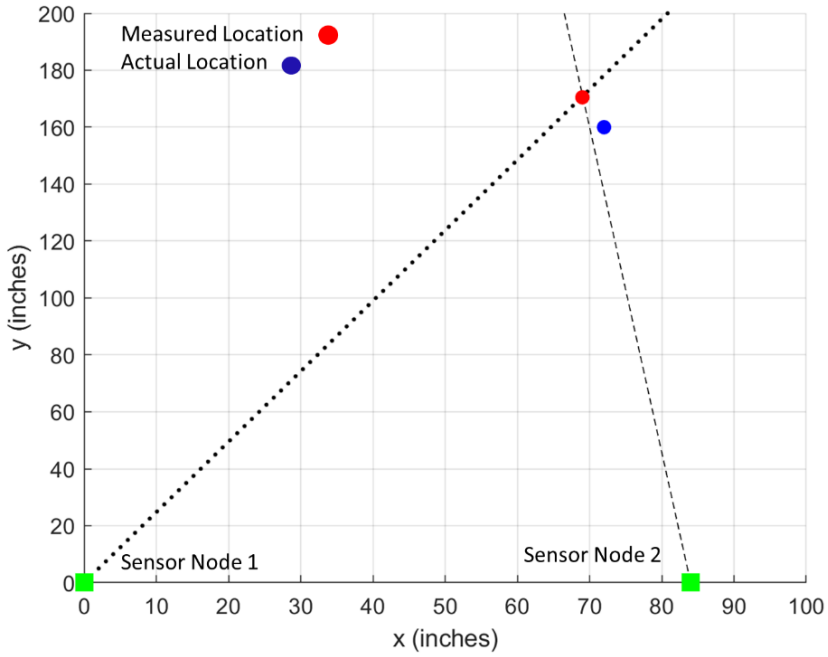

Figure 36. Triangulation output of test 1, trial 1 performed in MATLAB

Figure 37 and Table 8 are the results for all four trials of test 1. Figure 37 shows the mapping of the 4 measured locations of the sound source calculate by the intersection program in MATLAB. Table 8 displays the results. Trial 1 and 4 produced the same measured location of the sound source at grid point (69, 171) while trial 2 and 3 also produced the same measured location at grid point (66.8, 165). Using the Euclidean distance calculation, we computed the distance between the measured locations and the actual location at grid point (72, 160) (Wolfram MathWorld, n.d.). In the Euclidean formula, the actual location grid point is (x2, y2) and the measured location grid point is (x1, y1). The distances measured between the actual and measured in trials 1 and 4 is 11.40 inches while the distance in trials 2 and 3 is 7.21 inches, which show precision and accuracy.

$$Distance = \sqrt{(x_2 - x_1)^2 + (y_2 - y_1)^2} \quad (16)$$

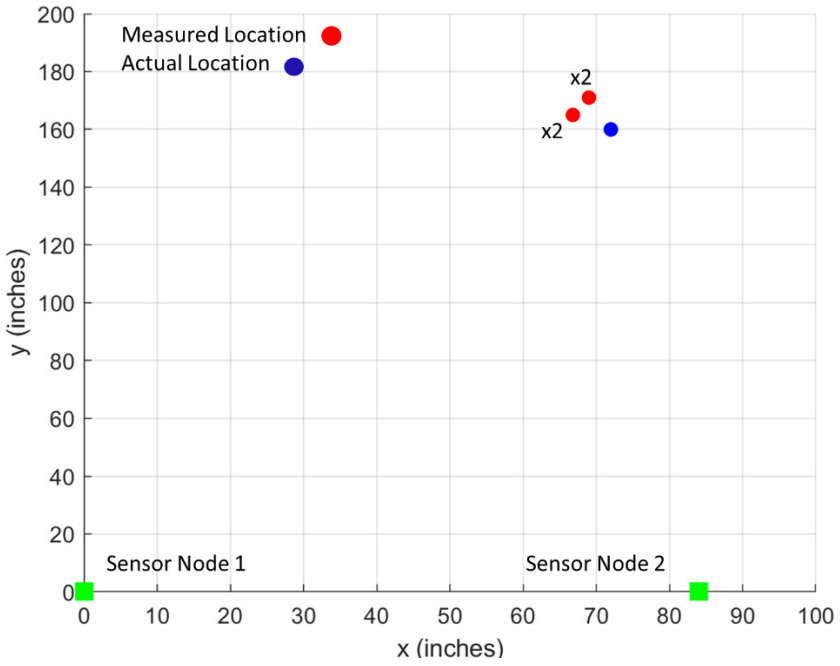

Figure 37. Overall results from MATLAB program triangulating the sound source for test 1, trials 1-4

Table 8. Results of anechoic chamber test 1 to include bearings from sensor nodes, measured location, and distance between measured and actual

	Anechoic Chamber Test 1						
	Sensor 1 Location (inch)	Sensor 2 Location (inch)	Sensor 1 Bearing	Sensor 2 Bearing	Measured Location (inch)	Actual Location (inch)	Distance Between Measured and Actual (inch)
Trial 1	(0,0)	(84,0)	22	-5	(69, 171)	(72, 160)	11.4018
Trial 2	(0,0)	(84,0)	21	-6	(66.8, 165)	(72, 160)	7.2139
Trial 3	(0,0)	(84,0)	21	-6	(66.8, 165)	(72, 160)	7.2139
Trial 4	(0,0)	(84,0)	22	-5	(69, 171)	(72, 160)	11.4018

b. Anechoic Chamber Triangulation Test 2

For the second test, sensor node 1 and the sound source are located at their stationary locations while sensor node 2 is located at grid point (52,0). Figure 38, Figure 39, and Table 9 are the results from the experiment from test 2 in the anechoic chamber. Figure 38 is an example of the output from test 2, trial 1 from the triangulation program implemented in MATLAB, which includes the bearing lines from each sensor node, the measured location of the sound source, and the actual location of the sound source. Figure

39 and Table 9 are the results for all four trials of test 2. Figure 39 shows the mapping of the 4 measured locations of the sound source calculate by the intersection program in MATLAB. Table 9 displays the data from results in MATLAB to include the bearings from each sensor node, the measured location, and the distance between the measured and actual location. From the results, the calculations in trial 1 produced the measured location of the sound source at grid point (64, 167) while trials 2, 3, and 4 had the same measured location at grid point (63, 157). The distances measured between the actual and measured in trial 1 is 10.63 inches while the distance in trials 2, 3, and 4 is 9.49 inches. Table 9 shows the results of the distances calculated using the Euclidean formula. Similar to the results in test 1, the measurements validate the accuracy and precision of the system.

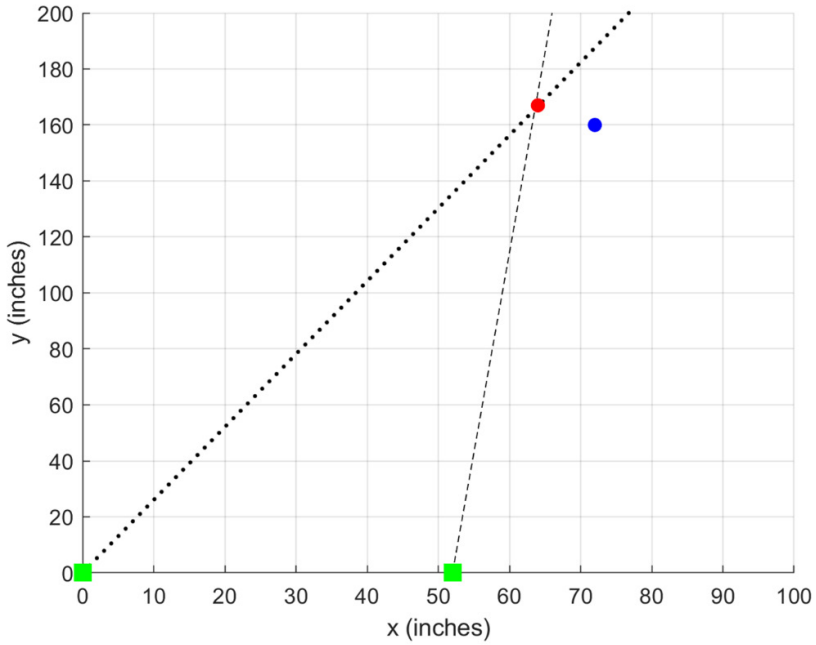

Figure 38. Triangulation output of test 2, trial 1 performed in MATLAB

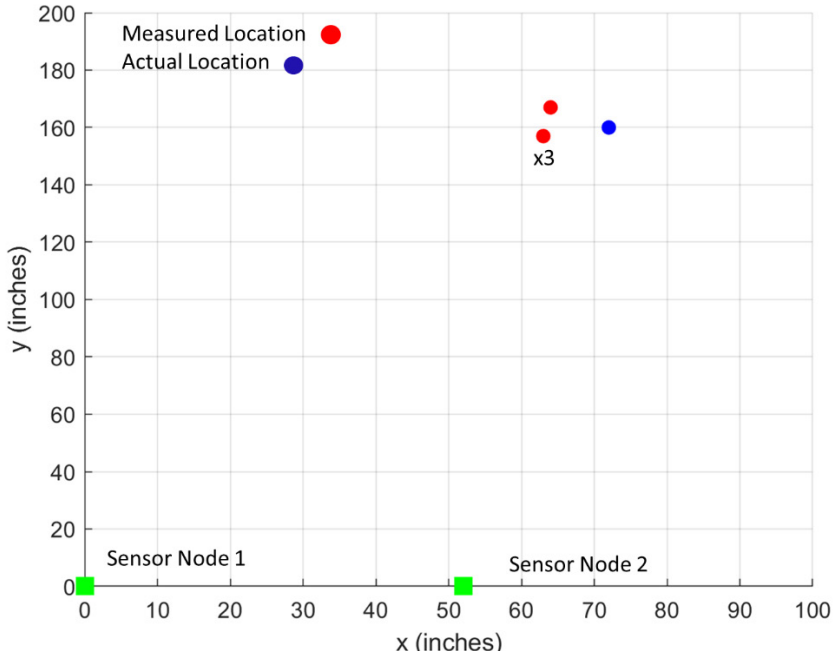

Figure 39. Overall results from MATLAB program triangulating the sound source for test 2, trials 1-4

Table 9. Results of anechoic chamber test 2 to include bearings from sensor nodes, measured location, and distance between measured and actual

	Anechoic Chamber Test 2						
	Sensor 1 Location (inch)	Sensor 2 Location (inch)	Sensor 1 Bearing	Sensor 2 Bearing	Measured Location (inch)	Actual Location (inch)	Distance Between Measured and Actual (inch)
Trial 1	(0,0)	(52,0)	21	4	(64, 167)	(72, 160)	10.6301
Trial 2	(0,0)	(52,0)	22	4	(63, 157)	(72, 160)	9.4868
Trial 3	(0,0)	(52,0)	22	4	(63, 157)	(72, 160)	9.4868
Trial 4	(0,0)	(52,0)	22	4	(63, 157)	(72, 160)	9.4868

c. Anechoic Chamber Triangulation Test 3

For the third test, sensor node 1 and the sound source are located at their stationary locations while sensor node 2 is located at grid point (90,0). Figure 40, Figure 41, and Table 10 are the results from the experiment from test 3 in the anechoic chamber. Figure 40 is example of the output from test 3, trial 1 from the triangulation program implemented in MATLAB, which includes the bearing lines from each sensor node, the measured location of the sound source, and the actual location of the sound source. Figure 41 and

Table 10 are the results for all four trials of test 3. Figure 41 shows the mapping of the 4 measured locations of the sound source compared to the actual location. Table 10 displays the data from results in MATLAB. The calculations in trial 1, 2, 3, and 4 produced the same measured location of the sound source at grid point (65.8, 171). The distances measured between the actual and measured from the four trials is 9.35 inches. Table 10 shows the results of the distances calculated using the Euclidean formula. These measurements also demonstrate the accuracy of the system from a different setup compared to the previous tests. The approximate location calculation is close to the actual location signifying the accuracy and since the results are close to another demonstrates the precision of the system.

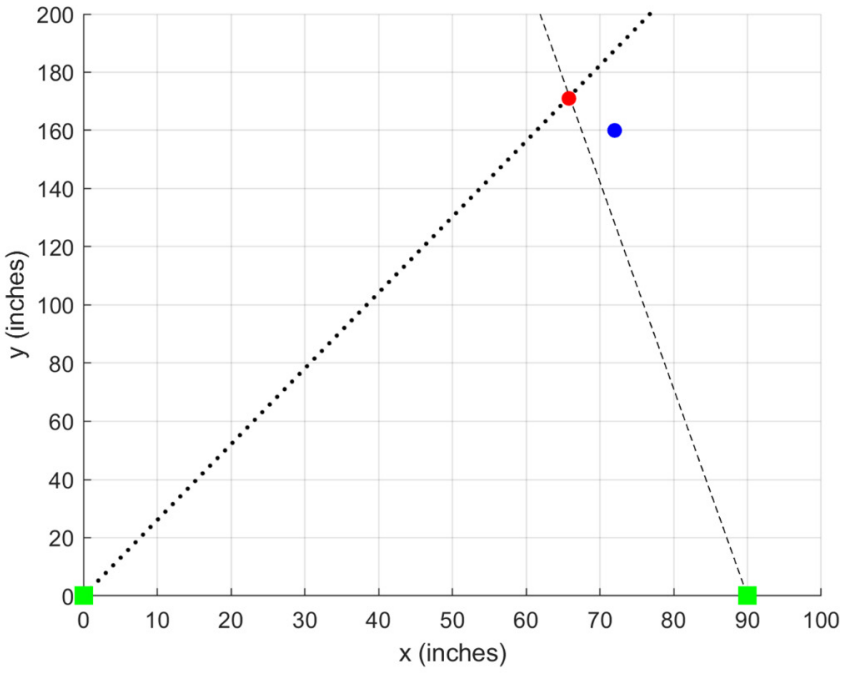

Figure 40. Triangulation output of test 3, trial 1 performed in MATLAB

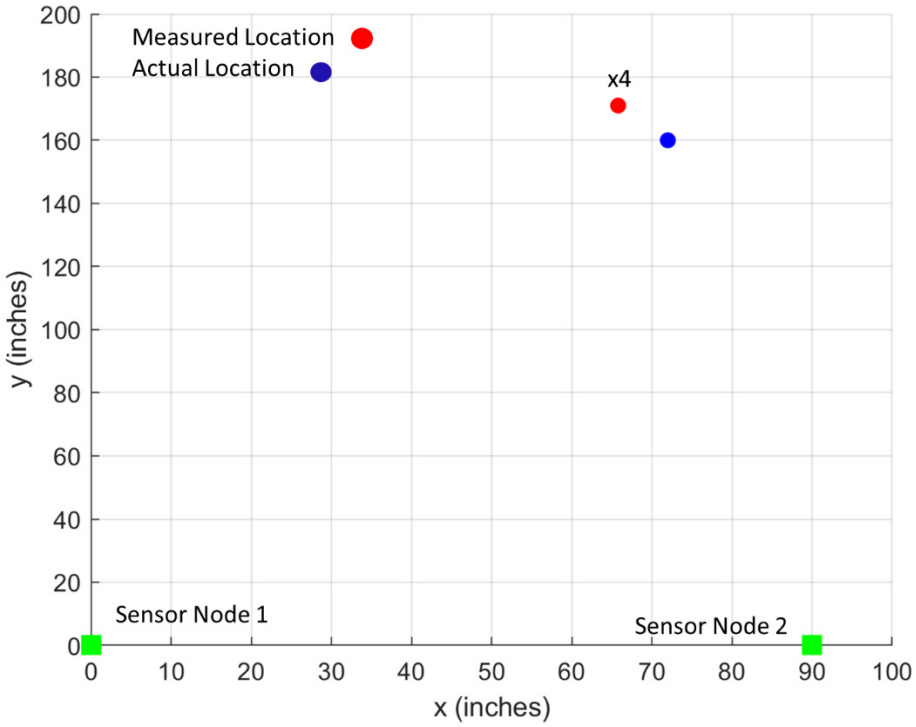

Figure 41. Overall results from MATLAB program triangulating the sound source for test 3, trials 1-4

Table 10. Results of anechoic chamber test 3 to include bearings from sensor nodes, measured location, and distance between measured and actual

	Anechoic Chamber Test 3						
	Sensor 1 Location (inch)	Sensor 2 Location (inch)	Sensor 1 Bearing	Sensor 2 Bearing	Measured Location (inch)	Actual Location (inch)	Distance Between Measured and Actual (inch)
Trial 1	(0,0)	(90,0)	22	-8	(65.8, 171)	(72, 160)	9.3509
Trial 2	(0,0)	(90,0)	22	-8	(65.8, 171)	(72, 160)	9.3509
Trial 3	(0,0)	(90,0)	22	-8	(65.8, 171)	(72, 160)	9.3509
Trial 4	(0,0)	(90,0)	22	-8	(65.8, 171)	(72, 160)	9.3509

3. Open Environment Testing

Outdoors tests were performed at the baseball field on the Naval Postgraduate School to evaluate the sensor system's response to the environmental factors. The size of the field and the acoustic intensity provided by the loudspeaker system limited the scale of the tests. Nevertheless, the field test still provided proof-of-concept and several insights for performance improvement and ruggedization of future prototypes. Figure 42 shows the

general setup with two sensor nodes and the acoustic source (speaker) source. The sound used for excitation was a recording of a bomb explosion, which is spectrally broad and contains the 1.6 kHz resonance frequency of the MEMS DF sensors. The sound source was played multiple times at two different distances to collect enough data to assess the system's output.

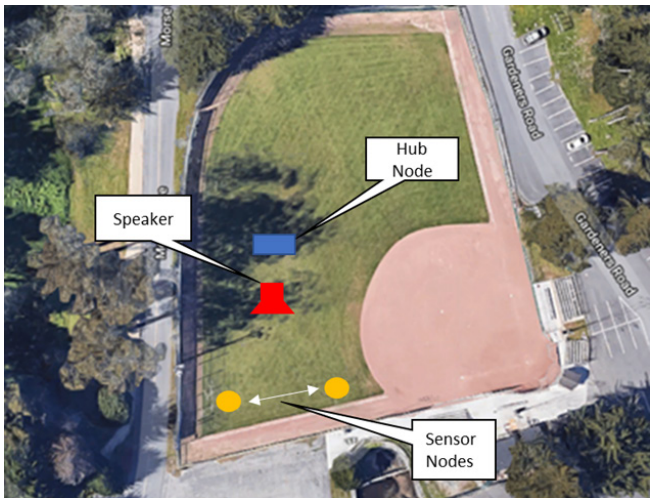

Figure 42. Overview of the general setup for the outside tests of the sensor system

a. Outdoors Triangulation Test 1

For the first test, sensor node 1 was placed 28 feet away from the speaker while sensor node 2 was placed 30 feet away. 18 data points were taken during the first test where the results can be viewed in Figure 43 and Table 11. Figure 43 is the collection of all measured locations, represented by the red crosses, that were calculated using the triangulation algorithm compared with the actual location represented by the blue circle. All the data points are plotted on an aerial view map with MATLAB. Figure 43 shows the precision of the sensor system in which all the measured locations are close in proximity with one another and close in distance to the actual location. Table 11 compares the measured latitude and longitude with the actual latitude and longitude. Using the haversine formula, demonstrated in Chapter III, paragraph C, part 1, we calculated the distance between the measured point and actual point to assess accuracy (Mahmoud & Akkari,

2016). The largest distance between the actual and measured was 24.3 feet (7.4 meters) with the closest distance to be 2.3 feet between the two points. The longer distances calculated were possibly the result of sound reflection off the surface, which the sensors received since they were close to the sound source. Only 5 of the 18 data points exceeded 20 feet between measured and actual positions while the rest of the points were less than 20 feet. The distances calculated are still ideal for Phase I of ADA since it provides a more accurate location with latitude and longitude coordinates than the current process. During the data collection, the nodes successfully transmitted their GPS location and bearing to the hub receiver for triangulation calculations.

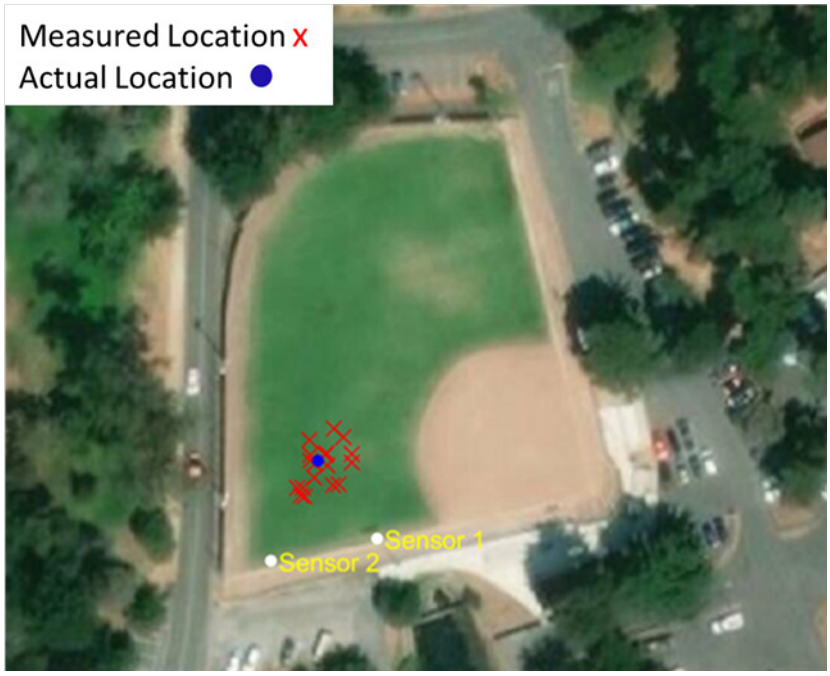

Figure 43. Aerial view of the measured points calculated by triangulation compared with the actual location

Table 11. Results of the measured coordinates compared with the actual coordinates and the distance between the two points

Test #	Trial #	Actual Latitude	Actual Longitude	Measured Latitude	Measured Longitude	Distance: Actual to Measured (meters)	Distance: Actual to Measured (feet)
1	1	36.597559	-121.870039	36.597571	-121.870020	2.1586	7.0820
	2	36.597559	-121.870039	36.597550	-121.870019	2.0472	6.7164
	3	36.597559	-121.870039	36.597559	-121.870055	1.4272	4.6824
	4	36.597559	-121.870039	36.597554	-121.870044	0.6976	2.2888
	5	36.597559	-121.870039	36.597568	-121.870022	1.8162	5.9587
	6	36.597559	-121.870039	36.597623	-121.870020	7.3156	24.0012
	7	36.597559	-121.870039	36.597556	-121.869966	6.5250	21.4076
	8	36.597559	-121.870039	36.597512	-121.870083	6.5382	21.4506
	9	36.597559	-121.870039	36.597594	-121.870058	4.2456	13.9293
	10	36.597559	-121.870039	36.597594	-121.870003	5.0477	16.5606
	11	36.597559	-121.870039	36.597499	-121.870075	7.4062	24.2985
	12	36.597559	-121.870039	36.597530	-121.870046	3.2845	10.7761
	13	36.597559	-121.870039	36.597512	-121.870070	5.9143	19.4037
	14	36.597559	-121.870039	36.597570	-121.869996	4.0300	13.2218
	15	36.597559	-121.870039	36.597614	-121.870005	6.8274	22.3997
	16	36.597559	-121.870039	36.597517	-121.870006	5.5226	18.1187
	17	36.597559	-121.870039	36.597568	-121.869995	4.0545	13.3023
	18	36.597559	-121.870039	36.597568	-121.870054	1.6715	5.4840

b. Outside Triangulation Test 2

For the second test, sensor node 1 was placed 37 feet away from the speaker while sensor node 2 was placed 39 feet away. The second test had 23 data points collected which can be viewed in Figure 44 and Table 12. Figure 44 is the aerial view of the measured locations compared with the actual location. 17 of the data points calculated by triangulation show accuracy and precision but there are 6 points that exceeded outside the range of the closer points. The 6 points indicating a false location were close together (systematic error), which indicates that the sensors were responding to reflection and the reverberation included in the recorded sound of the bomb blast. The 6 false readings are represented by yellow crosses while the accurate measured locations are red crosses in Figure 44. With more distance between the sensor nodes and the sound source, the nodes were able to detect and calculate the bearing with more precision than compared to the results in test 1. Viewing Table 12, the 6 false readings are highlighted in yellow to distinguish these points from the more accurate ones. 16 of the 17 positive readings were calculated to be less than 20 feet from the measured location to the actual location. The 16 accurate points also were in very close proximity of one another creating a tight measured

group. The sensor nodes also successfully transmitted data to the hub receiver for the triangulation and mapping.

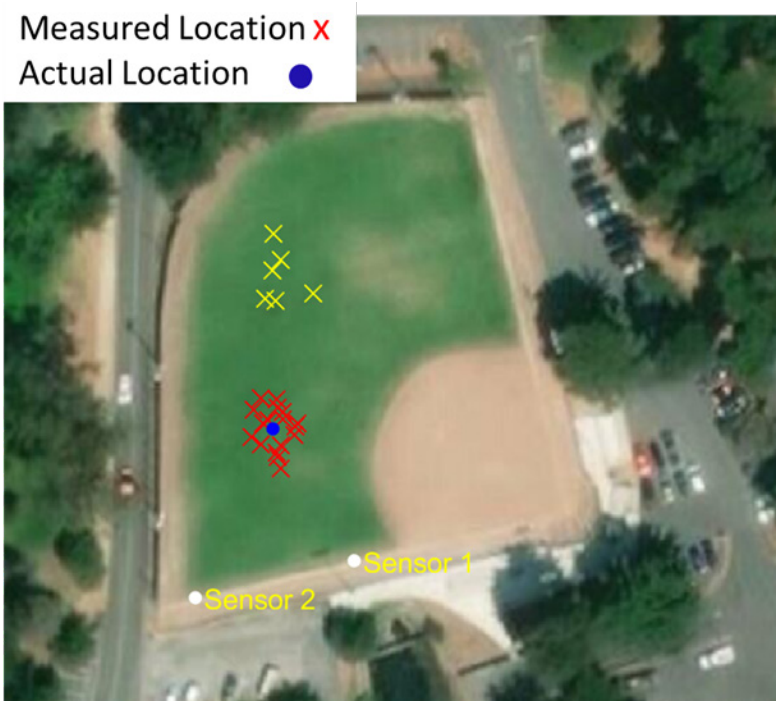

Figure 44. Aerial view of the measured points calculated by triangulation compared with the actual location

Table 12. Results of the measured coordinates compared with the actual coordinates and the distance between the two points

Test #	Trial #	Actual Latitude	Actual Longitude	Measured Latitude	Measured Longitude	Distance: Actual to Measured (meters)	Distance: Actual to Measured (feet)
2	1	36.597633	-121.870020	36.597641	-121.869973	4.2889	14.0713
	2	36.597633	-121.870020	36.597623	-121.869979	3.8246	12.5479
	3	36.597633	-121.870020	36.597572	-121.870005	6.9140	22.6837
	4	36.597633	-121.870020	36.597933	-121.870018	33.3590	109.4453
	5	36.597633	-121.870020	36.597658	-121.870000	3.3051	10.8434
	6	36.597633	-121.870020	36.597608	-121.870042	3.4045	11.1695
	7	36.597633	-121.870020	36.597832	-121.870034	22.1631	72.7135
	8	36.597633	-121.870020	36.597620	-121.870060	3.8516	12.6365
	9	36.597633	-121.870020	36.597892	-121.870005	28.8307	94.5887
	10	36.597633	-121.870020	36.597645	-121.870029	1.5599	5.1179
	11	36.597633	-121.870020	36.597666	-121.870011	3.7569	12.3256
	12	36.597633	-121.870020	36.597877	-121.870021	27.1320	89.0154
	13	36.597633	-121.870020	36.597589	-121.870011	4.9585	16.2680
	14	36.597633	-121.870020	36.597637	-121.869976	3.9532	12.9699
	15	36.597633	-121.870020	36.597830	-121.870014	21.9122	71.8903
	16	36.597633	-121.870020	36.597640	-121.870038	1.7837	5.8519
	17	36.597633	-121.870020	36.597647	-121.870000	2.3715	7.7805
	18	36.597633	-121.870020	36.597680	-121.870042	5.5827	18.3158
	19	36.597633	-121.870020	36.597678	-121.870012	5.0548	16.5840
	20	36.597633	-121.870020	36.597841	-121.869942	24.1539	79.2451
	21	36.597633	-121.870020	36.597607	-121.870005	3.1871	10.4562
	22	36.597633	-121.870020	36.597596	-121.870012	4.1772	13.7046
	23	36.597633	-121.870020	36.597662	-121.870056	4.5529	14.9375

C. SUMMARY

This chapter presented the findings and results from the experimentation in controlled and uncontrolled environment of the ground-acoustic sensor network system with only two nodes. The system was tested in the anechoic chamber with two different setups, which included testing the bearing accuracy of the MEMS DF acoustic sensor and the triangulation accuracy and precision of the ground sensor nodes. The bearing measurements were found to have errors, on average, less than 3 degrees when compared with the actual angles. The outside tests validated the capability of the sensor system for detecting and triangulating the sound source with environmental factors added. Though the testing scale was limited in size and the speaker's power level does not match that of an actual explosion, the system successfully proved the concept. The outside tests showed the measured locations in a close cluster for both tests. Most data points were within 20 feet of the actual location with only a few outside that range signifying the accuracy of the calculations. The transmission of data from the sensor nodes to the hub receiver for processing in MATLAB was also successful. The transmission of data during the tests

signifies the importance of the data communication during an actual bomb attack which, will increase the speed of Phase I of ADA. Testing shows that the sensor network system provides prominence in detecting and locating bomb impacts to support the ADA process. Chapter V provides the overall summary of the research and conclusions of the system as well as offers recommendations for future work.

THIS PAGE INTENTIONALLY LET BLANK

V. CONCLUSION

A. SUMMARY

Military airfields play an important role for power projection and sustainment for the U.S. military. The U.S. military conducts a wide range of operations to include combat operations, peacetime operations and exercises, and humanitarian assistance and disaster relief across the globe. Keeping the airfields operationally ready and running is important to the success of the operations of the U.S. military. ADA is vital to the successful conduct of ADR to restore an airfield after being damaged. To improve the ADA process, we designed and developed a real time, ground acoustic-sensor network to detect and triangulate the location of bomb impacts on an airfield. The goal of the system is to improve Phase I of ADA by using the sensor network to autonomously and instantaneously detect impacts while personnel are sheltering in place during an attack. The low-cost and low-power system made from COTS components provides the capability to execute the goal of the research. The sensor system is designed to enable personnel with limited technology experience to use the system in the operational environment and to assist with the execution of the ADA mission.

B. CONCLUSIONS

From the results gathered during the experimentation, the ground acoustic sensor network triangulates, within 20 feet, the location of a sound source to assist the ADA process. A current process used for assessing is the marker system that are in intervals of 50 or 100 feet. If personnel can assess the damage in referencing to the marker system, then they are able to accurately locate the damage within 100 feet. The sensor system can triangulate sound sources within 20 feet, which greatly improves the ability of pinpointing the location of a bomb impact as compared to conventional methods. The network system captures signals during an attack providing real-time data to the EOC. The system outputs the impact's latitude and longitude coordinates and displays them on a map, which assist the assessment teams to locate the damaged area and for the EOC personnel to track the

information. This system can reduce the search time for the ADATs since the location of the damage is already known, which has a positive impact on the ADA and ADR process.

C. RECOMMENDATIONS FOR FUTURE WORK

The research investigated the rapid triangulation of the location of bomb impacts on an airfield. Though the research proved that our system works, there are several recommendations for improving the system. There were constraints during the research to include the use of low cost COTS equipment and the testing environment for the system. Within these constraints, the system performed well and provided acceptable results in the anechoic chamber and the outside environment. The research lays the groundwork for the network system to be integrated with other sensor technology and UAVs to create a more capable system to further benefit ADA. To improve this system, additional research discussed below, should be considered.

The ground sensor nodes are typically positioned away from the airfield to get wider viewpoint and to avoid being hit. Though the sensor nodes are at some distance from the airfield, they are still subjugated to bomb explosions. The sensitivity and fragile sensors used in the system could be damaged by the explosion pressure. Also, the sensors deployed in an outside environment are susceptible to inclement weather and military operations being conducted. Some type of enclosure to protect the components from these aspects will ensure the longevity and accuracy of the device.

The experimentation was done in a controlled and an uncontrolled environment to assess the performance. However, to fully understand the equipment's performance and how it responds the natural elements, the network system should be tested in multiple operational environments. Also, the number of nodes should be increased to test the ability for more sensors to be on the network and significantly improve the accuracy of localization. This testing will improve the accuracy and capability of the ground sensor network to operate in an active military environment. During the tests, individual explosion sounds were used to validate the research. However, if an airfield is to come under attack, there will more likely be multiple munitions that will impact the runway. Research should be conducted on the system's ability to determine distinction between multiple impact

sounds occurring in rapid succession and provide that data to the hub node for triangulation calculations and accurate mapping.

The system supported our research goals but upgrades to some components should be researched to improve the performance. The system communication comprised of low-cost and low-power modules that created a simple yet effective network for transmitting data up to 800 meters line of site. Though this communication was reliable for testing, we must consider that airfields can reach up to lengths of 10,000 feet. Large airfields will require a more robust communication network to ensure proper data transmission. Also, security of the tested network system was not one of the research parameters but should be considered for future work to ensure the system is secure from service denial. Also, the microcontroller used in the sensor nodes was an Arduino Nano that was able to process the data captured by the sensors. For future work, a microcontroller with a higher clock speed should be used for processing, especially when we expect multiple blasts to happen in a short amount of time.

THIS PAGE INTENTIONALLY LEFT BLANK

APPENDIX. SOURCE CODE

Program code for the sensors, receiver, and MATLAB can be retrieved from the following link at the Naval Postgraduate School GitLab: https://gitlab.nps.edu/csnet/mwc/ADA/tree/master/CODE/Sensors%20and%20Triangulation. Users external to the NPS community should request access to the GitLab by contacting the NPS Computer Science Department.

THIS PAGE INTENTIONALLY LEFT BLANK

LIST OF REFERENCES

Federal Aviation Administration. (2016). *8260.58A - United States standard for performance based naviagtion (PBN) instrument procedure design.* Retrieved from https://www.faa.gov/regulations_policies/ordersnotices/index.cfm/go/document.information/documentID/1029267

Arduino. (2018, May 25). Arduino Uno Rev3. Retrieved from https://store.arduino.cc/arduino-uno-rev3

Atmoko, H. D. (2008, January 7). Accurate sound source localization in a reverberant environment using multiple acoustic sensors. *Measurement Science and Technology, 19*(2). Retrieved from https://iopscience.iop.org/article/10.1088/0957-0233/19/2/024003/pdf

Circuit Basics. (n.d.). Basics of the SPI communication protocol. Retrieved from http://www.circuitbasics.com/basics-of-the-spi-communication-protocol/

Brouwers, J. (2016, Mar 6). PyGeodesy. Retrieved from https://github.com/mrJean1/PyGeodesy

Brown, K. (2008). The role of Air Force civil engineers in counterinsurgency operations. *Air & Space Power Journal,* 22 (2), 44-50. Retrieved from https://search.proquest.com/docview/217772714/abstract/4548A696F5C443E6PQ/1

Carlson, G. (2002). Experimental errors and uncertainty. Retrieved from https://www.scribd.com/document/72394782/Error-Uncertainty

Clark, S. M. (2018). *Leveraging unmanned aeriel systems to modernize airfield damage assessment.* (Master's thesis). Retrieved from https://apps.dtic.mil/dtic/tr/fulltext/u2/1056460.pdf

Davis, N. J. (2018). *Expeditionary logistics: a low-cost, deployable, unmanned aerial system for airfield damage assessment.* (Master's thesis). Retrieved from https://apps.dtic.mil/docs/citations/AD1069529

Department of the Air Force. (2016). A*irfield damage assessment after major attack* (AFTTP 3-32.11). Washington, DC: Author Retrieved from http://www.wbdg.org/FFC/AF/AFTTP/afttp_3_32.11.pdf

Department of the Air Force. (2012). *Airfield damage repair operations* (AFPAM 10-219). Washington, DC: Author. Retrieved from https://www.wbdg.org/ffc/af-afcec/pamphlets-afp-and-afpam/afpam-10-219-v4

Gade, K. (2010). A non-singular horizontal hosition representation. *The Journal of Navigation, 63*(3), 395-417. Retrieved from https://www.navlab.net/Publications/A_Nonsingular_Horizontal_Position_Representation.pdf

Gerez, S. H. (2016). Implementation of digital signal processing: some background on GSFK modulation. Classnotes for Implementation of Digital Signal Processing, University of Twente, Enschede, Netherlands. Retrieved from https://wwwhome.ewi.utwente.nl/~gerezsh/sendfile/sendfile.php/gfsk-intro.pdf?sendfile=gfsk-intro.pdf

Hamilton, R. (2012, December 20). The darkroom: exploring visual journalism from the Baltimore sun. *Baltimore Sun*. Retrieved from http://darkroom.baltimoresun.com/2012/12/dec-20-photo-brief-snow-in-the-midwest-high-stepping-in-afghanistan-window-washing-santas-and-senator-inouyes-last-trip-to-the-capitol/an-unexploded-ordnance-is-seen-in-the-ain-terma-area-in-ghouta-east-of-damascus/

Karunasiri, G. & Downey, R.H. (2014). Reduced residual stress curvature and branched comb fingers increase sensitivity of comb fingers increases sensitivity of MEMS acoustic sensor. *IEEE Journal of MEMS, 23*(2), 417-423. https://ieeexplore.ieee.org/document/6595588

Karunasiri, G., & Alves, F. (2017). *United States Patent No. 9843858B1*. Washington, D.C: U.S. Patent and Trademark Office. Retrieved from https://patents.google.com/patent/US9843858B1/en

Karunasiri, G., Swan, W., & Alves, F. (2017). MEMS direction finding acoustic sensor. *Proceedings of SPIE, 10246*(6). Retrieved from https://calhoun.nps.edu/handle/10945/60304

Last Minute Engineers (n.d. -a). In-depth: How nRF24L01 wireless module works & interface with Arduino. Retrieved from https://lastminuteengineers.com/nrf24l01-arduino-wireless-communication/

Last Minute Engineers. (n.d -b). Interface ublox NEO-6M GPS module with Arduino. Retrieved from https://lastminuteengineers.com/neo6m-gps-arduino-tutorial/

Mahmoud, H., & Akkari, N. (2016). Shortest path calculation: a comparative study for location-based recommender. *2016 World Symposium on Computer Applications & Research*, 1-5. https://ieeexplore.ieee.org/document/7791971

McNeely, E. (2018). *Airfield damage assessment using light detecting and ranging (LIDAR)*. (Master's thesis). Retrieved from https://calhoun.nps.edu/bitstream/handle/10945/61225/18Dec_McNeely_Eric.pdf?sequence=1&isAllowed=y

Miles, R.N., Robert, D., & Hoy, R.R. (1996). Mechanically coupled ears for directional hearing in the parasitoid fly *Ormia ochracea*. *The Journal of the Acoustical Society of America*, *98*(6), 3059-3070. https://doi.org/10.1121/1.413830

MicroSensors, Inc. (2001). MS3110 universal capacitive readout IC datasheet. Retrieved from https://docplayer.net/39333632-Ms3110-universal-capacitive-readout-tm-ic.html

Nordic Semiconductor. (2008, March). nRF24L01+ single chip 2.4ghz transceiver datasheet. Retrieved from https://lastminuteengineers.com/datasheets/nrf24L01+2.4ghz-transceiver-datasheet.pdf

PRIME Faraday Partnership. (2002). *PRIME faraday technology watch: an introduction to MEMS*. Retrieved from https://www.lboro.ac.uk/microsites/mechman/research/ipmktn/pdf/Technology_review/an-introduction-to-mems.pdf

Random Nerd Tutorials. (2017). Guide to NEO-6M GPS module with Arduino Retrieved from https://randomnerdtutorials.com/guide-to-neo-6m-gps-module-with-arduino/

Simsek, K. (2009). *Developing a capacitance readout circuitry for a directional MEMS sound sensor and sound source socalization in a sensor network environment.* (Master's thesis). Retrieved from https://calhoun.nps.edu/handle/10945/4307

Stratech Systems Limited. (n.d.). Stratech systems intelligent vision: the future of homeland security today. Retrieved from http://www.thestratechgroup.com/iv_main.asp

Touse, M., Sinibaldi, J., Simsek, K., Catterlin, J., Harrison, S., & Karunasiri, G. (2010). Fabrication of a microelectromechanical. *Applied Physics Letters 96*(17). Retrieved from https://calhoun.nps.edu/handle/10945/60333

u-blox. (2011, May 12). NEO-6 u-blox 6 GPS modules data sheet . Retrieved from https://lastminuteengineers.com/datasheets/NEO-6M-GPS-DataSheet.pdf

United States Government. (2018). GeoExPT [Computer software]. Retrieved from http://www.geoexpt.com

United States Marine Corps. (2015, March 1). *Airfield damage repair (ADR) student outline* (instruction C-12B05). Camp Lejeunce, NC: Author.

United States Marine Corps. (2016, May 2). *Aviation ground support* (MCWP 3-21.1) Washington, DC: Author. Retrieved from https://www.globalsecurity.org/military/library/policy/usmc/mcwp/3-21-1/index.html

United States Naval Academy. (2017, October 12). Approximate metric equivalents for degrees, minutes, and seconds. Retrieved from https://www.usna.edu/Users/oceano/pguth/md_help/html/approx_equivalents.htm

Veness, C. (2019, February 1). Calculate distance, bearing and more between latitude/longitude point*s*. Retrieved from Movable Type Ltd: https://www.movable-type.co.uk/scripts/latlong.html

Williams, E. (2012, July 25). Aviation formulary . Retrieved from http://www.edwilliams.org/avform.htm#GCF

Wilmott, D. (2015). *Direction finding using multiple MEMS acoustic sensors*. (Master's thesis). Retrieved from https://calhoun.nps.edu/handle/10945/47345

Wilmott, D., Alves, F., & Karunasiri, G. (2016). Bio-inspired miniature direction finding acoustic sensor. *Scientific Reports 6*, 1-8. https://www.nature.com/articles/srep29957

Wolfram MathWorld. (n.d.). Distance. Retrieved from http://mathworld.wolfram.com/Distance.html

INITIAL DISTRIBUTION LIST

1. Defense Technical Information Center
   Ft. Belvoir, Virginia

2. Dudley Knox Library
   Naval Postgraduate School
   Monterey, California